Utrecht University

Faculty of Science

Measurement of displaced D^{*+}-mesons with the ALICE detector

Bachelor Thesis

Folkert Kuipers

Department of Physics and Astronomy

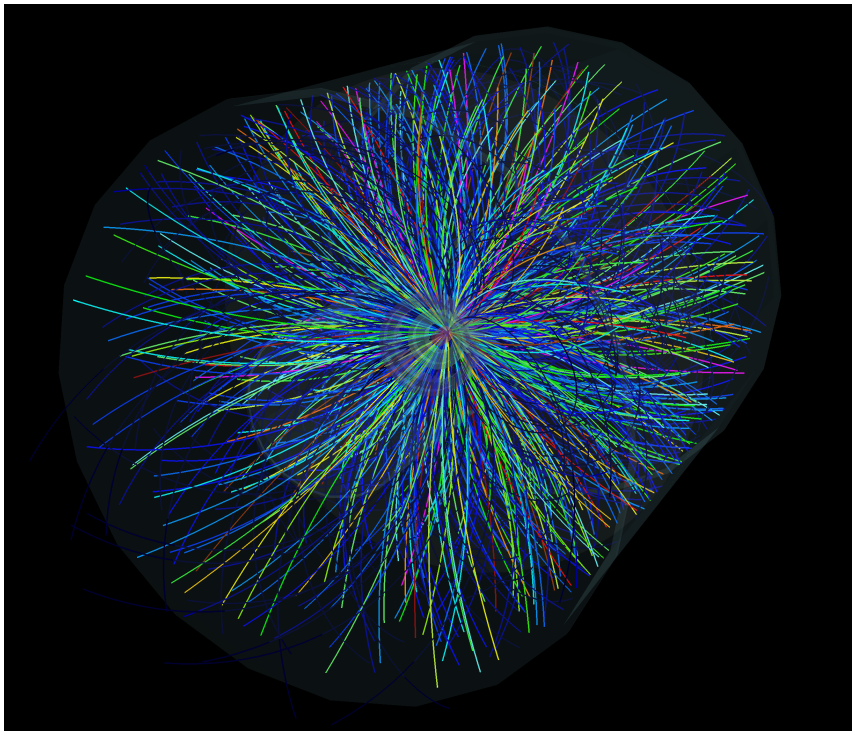

Supervisors:
Dr. Alessandro Grelli
Dr. André Mischke
Institute for Subatomic Physics

June 17, 2015

Abstract

Theories predict that shortly after the big bang the universe was filled with a phase of matter known as the quark-gluon plasma. The quark-gluon plasma is predicted by Quantum Chromodynamics, and only exists for very high densities and/or temperatures. Nowadays, these conditions can be reached in particle colliders such as the Large Hadron Collider at CERN. Experiments with the ALICE detector focus on studying the properties of this quark-gluon plasma. One of the ways to study the quark-gluon plasma is by looking at the difference of the properties of B-mesons that travel through a quark-gluon plasma and those who do not travel trough it. A quark-gluon plasma is created at high energy Pb-Pb collisions, but not in p-p collisions. For this thesis, a Monte-Carlo data set of p-p collisions at 7 TeV is analyzed. We focus on the D^{*+}-meson that is created in these interactions. The D^{*+}-mesons can be produced by a charm quark (prompt) or by the decay of a B-meson (feed-down), which itself is produced by a beauty quark. The purpose of this study is to separate these two different decay channels. In order to do this, we make use of the fact that feed-down mesons are displaced (i.e. they are not created at the collision point). By reconstructing the D^{*+}-mesons we can find their impact parameter, which is expected to be higher for feed-down mesons. In this study, this has been verified, and cuts on impact parameter have been applied. The cuts have been applied on the impact parameter of the pions and kaons, which are decay products of the D^{*+}-meson. The study has been performed for different p_T bins of the D^{*+}-meson. By applying the cuts on impact parameter, it turns out that we are able to increase the ratio of feed-down D^{*+}-mesons up to 100%. For higher p_T of the D^{*+}-meson, the cuts are more efficient. By applying these cuts on real data, we will be able to study the B-meson in p-p collisions. A small outlook is given in this thesis, where expectations for the cuts in Pb-Pb collisions in the new detector setup of ALICE are discussed.

[0]Figure on the title page shows the ALICE event display of one of the first lead ion collisions on November 8, 2010 [1]

Contents

Abstract **1**

Preface **3**

1 Introduction **4**
1.1 A brief history of subatomic physics 4
1.2 The Standard Model 5
1.3 Quantum Chromodynamics 6
1.4 Quark-Gluon Plasma 7
1.5 Heavy quarks and their interaction with QGP 8
1.6 Production and decay of D^{*+}-mesons 9

2 Experimental setup **11**
2.1 The ALICE detector 11
2.1.1 Inner Tracking System 11
2.1.2 Time Projection Chamber 13
2.1.3 Time of Flight detector 14
2.2 Analysis framework 15

3 The Monte-Carlo data set and analysis method **16**
3.1 The decay channel 16
3.2 Analysis of the data sample 16
3.3 Invariant mass reconstruction 17
3.4 Transverse momentum distributions of the D^{*+} and B-mesons 19

4 Cuts on impact parameter **22**
4.1 Impact parameter distributions of the D^{*+} and its daughters 22
4.2 Purity of the sample after applied cuts 30

5 Discussion and Conclusions **34**

6 Outlook **35**
6.1 Comparison with Pb-Pb data at 5.5 TeV 35
6.2 Future studies 36

Appendix A Invariant mass distributions in p_T bins of the D^{*+} **37**

Appendix B Momentum distributions of the D^{*+} daughters **40**

Appendix C Resolution of the detector **42**

Bibliography **44**

Preface

The main topic of this thesis is the study of the production of D^{*+}-mesons in proton-proton and lead-lead collisions in the ALICE detector at CERN. There are two main production channels for D^{*+}-mesons: they can be produced from a charm quark or from a B-meson, which itself comes from a beauty (bottom) quark. The main purpose of this thesis is to find a way to separate data from these two D^{*+}-mesons and the background signal. After this separation has been made I will discuss the effectiveness of the separation. If we will be able to make an effective separation in this data, this will provide a good way to study the properties of the charm and beauty quarks separately. These properties will provide more insight in the properties of the quarks themselves and the quark-gluon plasma. The study in this thesis can, therefore, contribute to a better comprehension of the standard model of particle physics, which is the most fundamental model we have so far for all the visible matter in the universe. Moreover, this study can provide more insight in the early stages of the universe, since, according to modern physical theories, shortly after the big bang, all visible matter consisted of a quark-gluon phase.
In order to make the separation in the ALICE data, I will study a Monte-Carlo simulation of proton-proton interactions in the 2010 setup of the ALICE detector. This studies will propose a way to cut in the data from ALICE. After this, I will compare the proton-proton simulation with a simulation of lead-lead interaction in the upgraded ALICE detector, which will run in about 4 years from now. From this comparison I will give a rough estimate of the improvement that can be made with the new detector setup.
The subject of the thesis is an experimental study of a very tiny part of the research that is done within the context of subatomic physics. Subatomic physics itself is one of the many branches within physics, and is mainly concerned with the question about the fundamental building blocks of all the matter in nature. The length scale of this fundamental particles is roughly 10^{-15} m (size of protons and neutrons) and smaller.
Before, I will get to the main topic of this research and the results of my research, I will give a short introduction into the subatomic physics. This introduction will start with a short history, and go along the standard model, quantum chromodynamics, heavy flavor production to the production and decay of D^{*+}-mesons. After this introduction, I will describe the most important aspects of the ALICE detector and the analysis framework Root, which has been developed at CERN.

1 Introduction

1.1 A brief history of subatomic physics

Subatomic physics is just like all branches of science the result of centuries of questioning, thinking and experimenting. Years of research have made subatomic physics a branch of its own in the big tree of all sciences, which is rooted in philosophical questions mankind has asked himself for thousands of years. In what follows, I will give a short and very incomplete overview of the history of subatomic physics, because we would never be, where we are now, without the effort and time that has been invested by other researchers.[1]
One could say that subatomic physics started from the moment people formulated questions about the nature of matter. Nobody knows, when exactly people started to ask these kind of questions, but we can be sure that mankind has asked them for a very long time already. We also know that people have tried to formulate reasonable or logical answers to these questions. It is very well known that in the Greek classical period, it was a very popular idea to consider fire, water, earth and air as the 4 fundamental elements. During the same period, Demokritos and Leucippus argued that all matter is build from small elements, which contains fundamental properties of the matter itself. Although, one could see some comparisons between the 'atomos' in Demokritos' theory and the molecules and atoms that we know today, and between the classical elements and four phases (solid, liquid, gas and plasma) matter can be in, these ideas could not be proved until people started to do experiments in the 17th century.
In the 17th and 18th century, experiments were done that indicated the existence of atoms and molecules. It took until the late 19th century, however, that people discovered that atoms were not the smallest particles in nature. In 1897, Thomson performed experiments that indicated the existence of very small particles with a negative charge, that were much lighter than atoms. These particles are now known as electrons. Later, Rutherford's experiments pointed to the existence of very small and heavy nuclei of atoms, which have been put in an atomic model by Niels Bohr. Afterwards, the existence of the proton and in 1932 the neutron was shown in experiments. The model of an atom with electrons, protons and neutrons gave a quite satisfying theory about the fundamental matter.
In the early 20th century, questions about the nature of light led to the birth of quantum mechanics. Also, experiments proved that there should be something like a photon, which is yet another fundamental particle. Shortly after, lots of experiments, especially the study of cosmic rays and the first collision experiments, showed that there had to exist even more particles, like mesons. In the next fifty years, a lot of theoretical and experimental work has been done by many researchers leading to what we now know as the standard model of particle physics. In these years, new particles were found in experiments, and showed the need for new theories. On the other hand, theories often predicted particles that later were found in experiments. The detection of these particles became a tough job, since the energy needed in collisions to detect the particles has to be very high. This led to the construction of many different kinds of particle detectors and particle accelerators, of which the Large Hadron Collider (LHC) at the Conseil Européen pour la Recherche Nuclaire (CERN) in Geneva is the most famous and the most important for this thesis.
Although the standard model is now 'complete', still a lot of research on the properties of all the particles that exist within the framework of the standard model is conducted. Also, it turns out that the standard model is not able to describe all observed processes on the small scale. Hence, there is still a lot of research to be done in the coming years.

[1] The overview that follows is largely based on [2] and [3].

1.2 The Standard Model

As mentioned in the last paragraph, the standard model of particle physics is the model that describes all the now known fundamental particles, and is a result of half a century of very active research. In this section, a brief overview of the most basic and most important features of the standard model is given.[2]

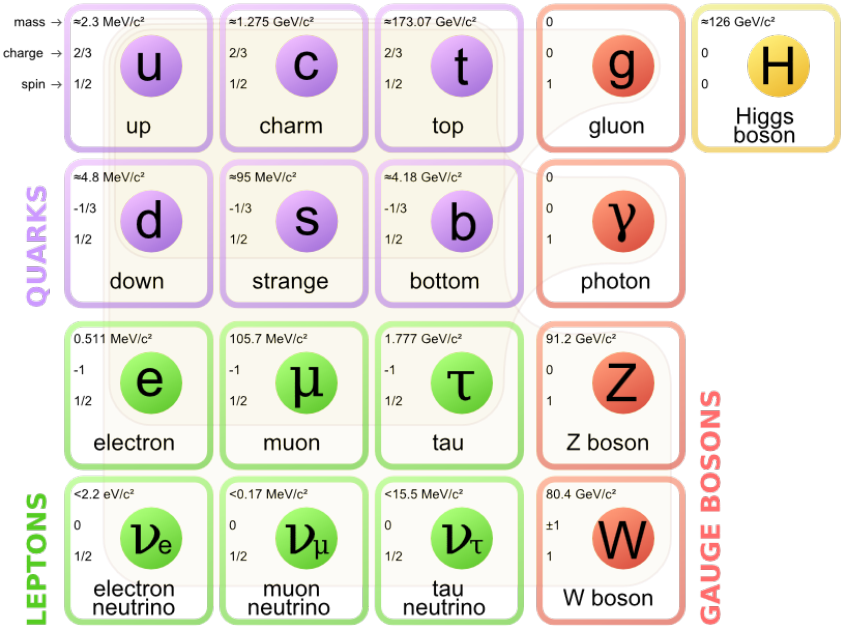

Figure 1.1: The standard model of particle physics [5].

The standard model is schematically illustrated in figure 1.1. In this figure, the most fundamental particles (as far as we know) are shown. It should be noticed that most of the particles shown in this figure also have an antiparticle, which is a particle with the same spin and mass but with opposite values for the other quantum numbers (charge, isospin etc.). As mentioned earlier, the standard model does not describe all physics on small scales. The standard model is namely not able to explain gravity, and is even incompatible with general relativity [6]. Therefore, physicists are looking for new models like the string theory and the Grand Unified Theory that go beyond the standard model. However, the standard model as it is now allows us to understand a lot of processes on the small scale. (In what follows, when I talk about fundamental particles I mean the fundamental particles of the standard model shown in figure 1.1.) The standard model divides the fundamental particles in two main categories: bosons and fermions.
Bosons have an integer spin. The gluon is a massless and chargeless boson, that is related to the strong interaction. The photon is also massless and chargeless, but is the force carrier of the electromagnetic interaction. The weak interaction is mediated by the Z, W^+ and the W^- bosons. The W^+ and its antiparticle the W^- are charged particles, while the Z is neutral. Together these bosons form the group of gauge bosons which carries 3 of the 4 'fundamental forces'. The Higgs boson is a recently measured boson that is responsible for the Higgs field, which explains why particles have mass.[3]
The second major category of fundamental particles is formed by fermions. Fermions have half integer spin and are the building blocks of all visible matter in nature. Fermions them-

[2] This section is largely based on the description of the standard model given by [4].
[3] A detailed description of all the bosons, and in particular the Higgs boson, is out of the scope of this thesis.

selves are split into leptons and quarks. Leptons are divided in three families: the electron and electron neutrino, the muon and muon neutrino and the τ particle and the τ neutrino. Neutrinos are only affected by the weak interaction, and therefore, very hard to detect. τ particles, muons and electrons are a lot easier to detect, although only the electron is a stable particle. τ particles and muons decay into electrons.
The other category of fermions is formed by the quarks. The existence of quarks was first proposed by Gell-Mann and Zweig. The quarks were needed to describe the underlying physics of a mathematical model known as the Eightfold way. In this model, Gell-Mann described symmetries that he found in the bunch of particles that were discovered in the mid-20th century in particle accelerators and cosmic rays. In the first model Gell-Mann and Zweig only described three different quarks (quark flavors): up, down and strange. Soon after Glashow and Bjorken predicted the existence of a fourth quark, charm, to better describe the weak interactions. Later Kobayashi and Maskawa predicted the existence of 2 other quarks, top and bottom (also known as beauty). By now, all these quarks have been detected in particle accelerators. The first to be discovered were the up and down quarks in the Stanford Linear Accelerator around 1970 [7]. Around the same time Kobayashi and Maskawa predicted the existence of two extra quarks. After this a long time of experimenting was needed to discover the other quarks. Due to its large mass and short lifetime (about $10^{-24}s$ [7]), it took until 1995 to discover the top quark. The six quarks can be divided in three generations: up and down, strange and charm, top and beauty. The up-type quarks (up, strange and top) have a charge of $\frac{2}{3}e$ and the down-type (down, charm and beauty) have a charge of $-\frac{1}{3}e$.
Quarks can be combined to form hadrons, which can be divided into mesons and baryons, where mesons consist of a quark and an anti-quark, and baryons of three quarks or three anti-quarks. However, the building of hadrons from quarks could violate the Pauli exclusion principle, which states that there can not be two fermions in exactly the same state (i.e. all the quantum numbers are the same), if this would be the full story. A Δ^{++}-resonance for example consists of 3 up quarks that all have spin up. This problem can be solved by introducing a new quantum number to the quarks, which is known as the color charge. Quarks can have 6 different colors (red, green, blue and their anti-colors). Now the 3 up quarks with spin up can form a Δ^{++}-particle, when they have a different color. With the introduction of the color charge a lot of new mesons could be created. However, the color model adds the restriction that all hadrons have to be 'colorless'. This can be achieved for mesons by combining a color with its anti-color, and for baryons by adding all three colors (or anti-colors) together. The force that binds quarks is the strong interaction, and is best described by quantum chromodynamics, which is discussed in the next section.

1.3 Quantum Chromodynamics

Quantum Chromodynamics (QCD) is a theory that effectively describes the interactions between quarks and gluons. The theory is made in analogy with quantum electrodynamics (QED). In QED particles interact with each other, because of their charge, and the interaction is mediated by chargeless photons. In QCD, the equivalent to charge is the color of a quark and the mediator of the interaction is the gluon. One important difference with QED is that gluons also carry color charge. Gluons do not have one color like quarks do, but they have a superposition of colors. It turns out that gluons themselves can have eight different superpositions of colors [8]. Because gluons have a color charge themselves they interact with quarks and also with other gluons. This makes QCD dynamics more complicated than QED. However, this also explains the asymptotic freedom and confinement that exists in quantum chromodynamics.

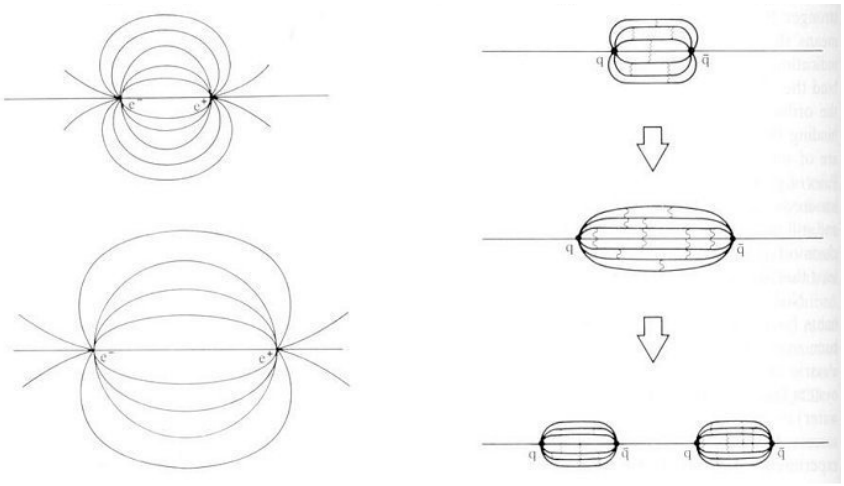

Figure 1.2: Field lines in QED (left) and QCD (right) when charges are separated [10].

The potential describing quantum chromodynamics can be written down analogous to the potential in QED [9]:

$$V_{QCD}(r) = -\frac{4}{3}\frac{\alpha_s}{r} + \kappa r. \tag{1}$$

The second term in this equation does not exist in the potential for QED. The term has the form of the potential energy in a string. This potential energy is known as the confinement term. This term scales with the κ and will increase the energy, when quarks are separated from each other. If the separation becomes to large (order of 10^{-15} m), this potential energy term will be large enough to form a new quark anti-quark pair. This also implies that in 'normal' circumstances quarks will never exist on their own. The process of creating a new quark anti-quark pair is shown in figure 1.2. In this description the field lines of the gluon field get closer to each other, when the quarks are separated. In contrast, the field lines of an electromagnetic field go further away from each other, when the charges are separated. The first term in the potential (equation 1) is a term that looks very much like the potential in QED. The fine structure constant is replaced by another constant α_s for which holds:

$$\alpha_s \propto \left(\ln \frac{|Q^2|}{\Lambda^2_{QCD}} \right)^{-1}, \tag{2}$$

where Q is the transfer of exchanged four-momentum and Λ_{QCD} is a experimental constant of about 300 MeV/c. For small distances, corresponding to small values of $|Q^2|$, α_s becomes small and quarks behave like free particles inside the hadron. This is called asymptotic freedom. For larger distances α_s becomes large. For large α_s perturbation theory cannot be used, and therefore, lattice QCD has been developed. This theory solves the equations of QCD numerically on lattice space-time [3]. The results of these calculations predict a phase transition of matter to a new phase known as the quark-gluon plasma.

1.4 Quark-Gluon Plasma

The quark-gluon plasma is a phase of matter that follows from the theory of quantum chromodynamics. This state only exists for very high densities and/or temperatures (figure 1.3). In a quark-gluon plasma quarks and gluons are no longer bound within hadrons and they are able to move around like free particles. Hence, in this state, quarks exist on their own in the sense that they are not bound to other quarks and gluons by their color charge. As mentioned in the previous chapter, this phenomenon is called asymptotic freedom. Theories

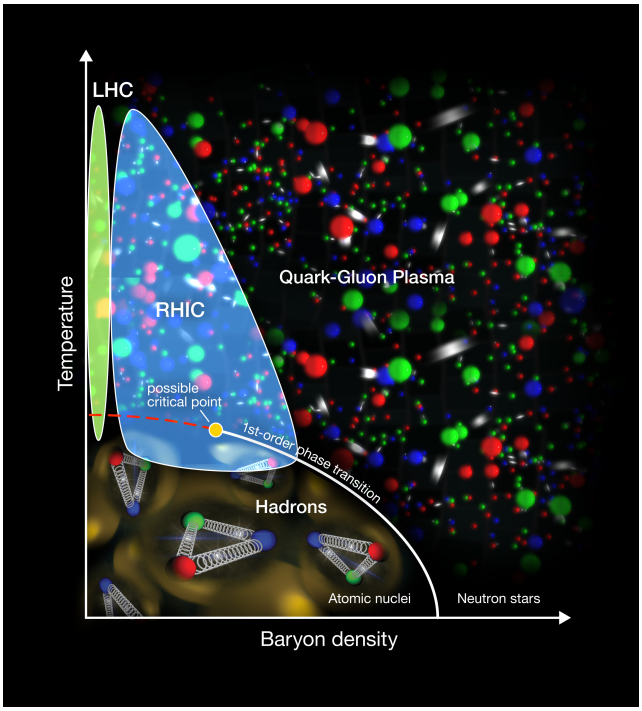

Figure 1.3: The phase diagram of quantum chromodynamics [11].

predict that in the early universe a few μs after the big bang, the universe was filled with a quark-gluon plasma [3]. Studying the quark-gluon plasma will, therefore, reveal information about the universe shortly after the big bang. Nowadays, the quark-gluon plasma can be reached in particle colliders. As shown in figure 1.3, we can reach the quark-gluon plasma now in the LHC at CERN in Geneva and in the Relativistic Heavy Ion Collider (RHIC) at Brookhaven National Laboratory (BNL) in the USA [11]. In the RHIC, this is done by colliding gold nuclei with an energy of 7.7 GeV. In the LHC, the quark gluon plasma is created in lead-lead collisions, and can exist for a longer time than in the RHIC [4]. In the first run of the LHC (2010-2013) the proton-proton collisions had a center of mass energy of 7 TeV and the lead-lead collisions a center of mass energy of 2.76 TeV in the second run which is planned for 2015-2018, the center of mass energies will be increased to 13 TeV and 5.5 TeV respectively.

When lead nuclei are accelerated to high velocities, length contraction will reshape the spherical nuclei to disks. These disks will collide, and have an overlapping region in the collision. The measure for this overlapping region is called the centrality. The centrality of collisions is experimentally expressed as a percentage of the total nuclear interaction cross-section [12]. Hence, for a Pb-Pb, it expresses collision how many of the nucleons are participating in the collision. A collision of the two lead nuclei will then form a quark gluon plasma as shown in figure 1.4. This plasma will only exist for a very short while, and cannot be observed directly, since it will be hadronized before it hits a detector.

1.5 Heavy quarks and their interaction with QGP

Within the quark-gluon plasma quarks and gluons move almost freely. Most of the quarks are light quarks (up and down). However, there are also some heavy quarks (strange, charm and beauty) created in the heavy ion collisions. Heavy quarks can be produced in several ways. A gluon can collide with another gluon and create a heavier quark anti-quark pair

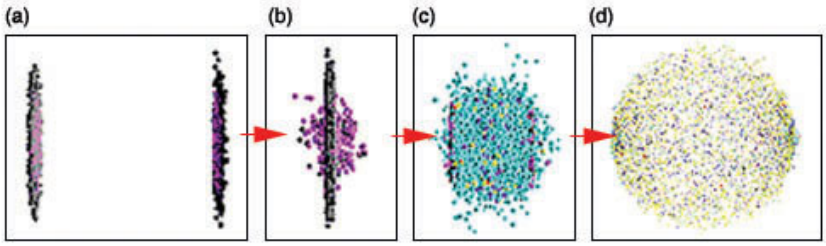

Figure 1.4: Stages in a head-on gold-gold collision. (a) Two nuclei approach one another with a speed near the speed of light. (b) The two nuclei collide, and pass through each other. Some of the energy is transformed into heat and new particles. (c) With the right conditions a quark gluon plasma is formed. (d) The system cools down and more hadrons are created. [13].

or a quark can annihilate with its anti-quark and form a heavy quark anti-quark pair [4]. The production time of the quarks is proportional to $\frac{1}{m_q}$ [14]. This implies: the heavier the quark, the faster it will be produced. This is why charm and beauty quarks are good probes to study the quark-gluon plasma [3]. They can experience the whole lifetime of the quark-gluon plasma (i.e. they are produced before the QGP is formed and decay afterwards).
In the quark-gluon plasma the quarks lose energy by radiating gluons. This radiation process is comparable to Bremsstrahlung: radiation of photons by electrons in an electro-magnetic field. The radiation of the gluons, however, is suppressed below a certain angle $\theta = \frac{m_q}{E_q}$. This angle is proportional to the mass of the quark. Therefore, the angle will be larger for heavier quarks. This effect is know as the dead-cone effect [15]. The dead-cone effect implies that for heavier quarks the gluon radiation is more suppressed. Hence, the heavier the quark, the less energy it will radiate away in the quark-gluon plasma.

1.6 Production and decay of D^{*+}-mesons

Beauty quarks radiate away less energy than charm quarks within the quark-gluon plasma. This means that the momentum distribution for beauty quarks will be less affected by the plasma than the momentum distribution of charm quarks. Although, we cannot study the quarks themselves directly, we can look at the decay products of the quarks and study their properties. These properties will be related to the properties of the quarks themselves, and will, therefore, allow us to investigate the properties of the quark-gluon plasma. In general, there are a lot of different ways, in which a quark can fragment. In this thesis, I will focus on a specific fragmentation of the charm and the beauty quark [16]:

$$\begin{aligned} c &\to D^{*+} + X \qquad\qquad BR = (27.6 \pm 3.4)\% \\ b &\to B \to D^{*+} + X, \end{aligned} \tag{3}$$

where B is a beauty meson (i.e. a meson consisting of a beauty quark and another anti quark or an anti-beauty and another quark or. The other quark can be up, down, strange or charm). The D^{*+} is an excited $c\overline{d}$ state. Of course, the B-meson and charm quark can also decay or fragment to the antiparticle $\overline{D}^{*+} = D^{*-}$, which is an excited $\overline{c}d$ state.
The X can be a lot of different particles. There are a lot of different ways in which a c or B can decay into a D^{*+}-meson, but I will not look into detail in this process. In this thesis, I will focus on the D^{*+}-meson that is coming from a B-meson (B feed-down) and the D^{*+}-meson that is coming from a charm quark (prompt). In order to do this, I make use of the difference in lifetime of the B-meson and the charm quark. The average lifetime of a B-meson is $1.5 \cdot 10^{-12}$s [17]. This means that a B-meson travels on average 450 μm with the

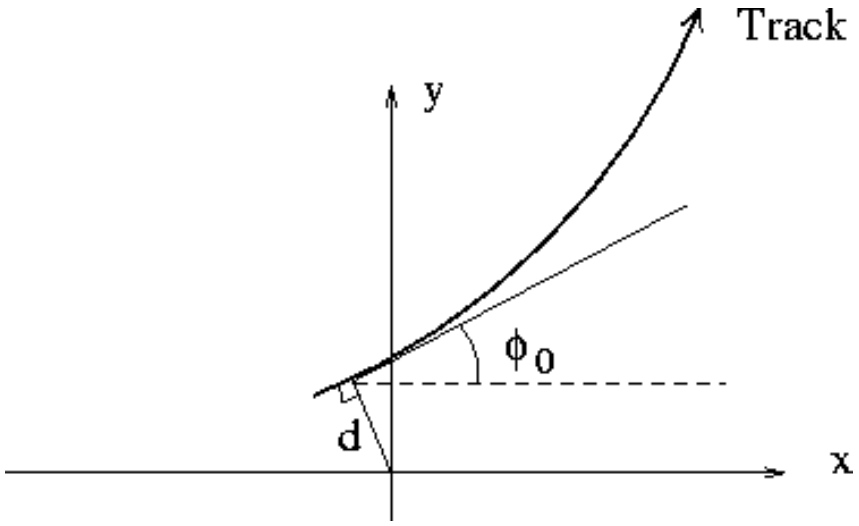

Figure 1.5: Illustration of the impact parameter, d, with respect to the origin as collision point [18].

speed of light. Not all the particles have the same lifetime and the mesons are traveling with a speed that is a little bit less than the speed of light, but the average distance a B-meson travels before decay is in the order of 100 μm. The lifetime of the charm quark is several orders of magnitude lower. Therefore, the D^{*+}-mesons coming from a B-meson decay will be produced further away from the primary vertex than the D^{*+}-mesons coming from a charm quark fragmentation. This implies that the measured impact parameter will, on average, be higher for D^{*+}-mesons coming from a B-meson than for the ones coming from a charm quark. For a reconstructed track, the impact parameter is defined as the distance of closest approach from the tangent line of the reconstructed track at the vertex, where it originates from, to the primary vertex (collision point). An illustration for the impact parameter is shown in figure 1.5.

Nuclear effects are typically quantified using the nuclear modification factor, given by equation 4 [3]. The nuclear modification factor is the normalized ratio between the yield in heavy-ion collisions and the yield in proton-proton collisions:

$$R_{AA}(p_T) = \frac{dN_{AA}/dp_T}{\langle T_{AA}\rangle d\sigma_{pp}/dp_T}, \tag{4}$$

where AA represents the particles that collide. In the LHC, AA would be Pb-Pb, and in RHIC it would be Au-Au. R_{AA} is the nuclear modification factor, T_{AA} is a nuclear overlap function, σ_{pp} is the production cross-section in proton proton interactions and $\frac{dN_{AA}}{dp_T}$ is the normalized yield.
If the core of a heavy ion is just a superposition of protons, the nuclear modification factor should be 1. The quark-gluon plasma is expected to lower this value, because of the energy loss in the quark-gluon plasma. (Note that a quark-gluon plasma can only be created in heavy ion collisions, not in p-p collisions.) Because the heavier beauty quark loses less energy due to radiation in the quark-gluon plasma than the lighter charm quark, one expects the R_{AA} value to be lower for the charm quarks than for the beauty quarks. In order to experimentally verify this, we have to be able to separate the data of the charm and the beauty quark in the ALICE experiment.

2 Experimental setup

The experimental setup used for this research is located at CERN (Conseil Européen pour la Recherche Nucléaire) in Geneva. CERN is a European research institute that was founded in 1954 by 12 states. Nowadays, CERN has 21 member states and a lot of countries inside and outside of Europe that contribute to the projects at CERN. At CERN scientists and engineers are collaborating to investigate the fundamental structures of the universe. In order to do this, there are many particle accelerators and detectors at CERN. In this chapter I will focus on the LHC (Large Hadron Collider), which is the largest particle accelerator in the world and has a length of 27 km. Before particles enter the LHC, they are already accelerated by other accelerators.
In the LHC, the particles are then accelerated to even higher energies (a few TeV), and they collide at several places within the LHC tunnel. In the LHC, there are 7 distinct experiments. All have their own particle detectors at a different location in the LHC. The two largest experiments are ATLAS and CMS, which are the most 'general' experiments and can investigate a large range of physics. The smallest experiments are TOTEM and LHCf, which focus on protons and lead ions that do not collide head on, but brush past each other. The detectors of TOTEM are build close to the CMS detector on both sides, and the detectors of LHCf are build close to ATLAS on both sides. Two other important detectors are the ALICE and the LHCb, which are more specialized then the ATLAS and CMS experiment. Finally, the MoEDAL experiment is build close to the LHCb, and looks for magnetic monopoles [19].

2.1 The ALICE detector

The analysis in this thesis is done for the ALICE experiment. The collaboration for the ALICE experiment consists of over a thousand scientists from 100 different institutes in 30 different countries. The main purpose of the ALICE experiment is the study of heavy ion collisions and the quark-gluon plasma that forms in these collisions. The ALICE detector is located 56m below ground, is $26 \times 16 \times 16$ m^3 and weighs 10000 tonnes. The ALICE detector consists of 19 different subdetectors, which all measure properties of the particles that are created in the collisions and fly through the ALICE detector. A schematic overview of the ALCIE detector is depicted in figure 2.1.
The ZDC's, FMD, V0 and T0 detectors are used together to reconstruct the initial conditions of the collisions, i.e. the amount of energy, the location and the time of collision. Around the particle beam there are cylindrical detectors (ITS, TPC and TRD), which are used to track the particles with electric charge. These 'tracking' detectors are located in a magnetic field of $B = 0.5$T, which bends the trajectories of the particles. The measured curvature of the tracks is used to find the momentum of the particles. Other detectors like PHOS, PMD and EMCal are used for the measurement of photons. In addition, EMCal is also used to measure photons and jets of particles.

The cylindrical detectors have a coverage over a full azimuthal angle and over a pseudo-rapidity $|\eta| < 0.9$, which means that they detect particles that fly under a polar angle of $45° < \theta < 135°$ with the beam line (which is taken to be the z-axis). For the reconstruction of the D^{*+}-mesons, the ITS, TPC and TOF subdetectors are most important and will be discussed further in the next subsections.

2.1.1 Inner Tracking System

The inner tracking system (ITS) is a cylindrical detector closest to the beamline (about 3cm from the beamline [3]). The main quality of the ITS is that it can measure the vertex, from which a particle passing through the ITS originates, up to an accuracy of 0.1 mm. This

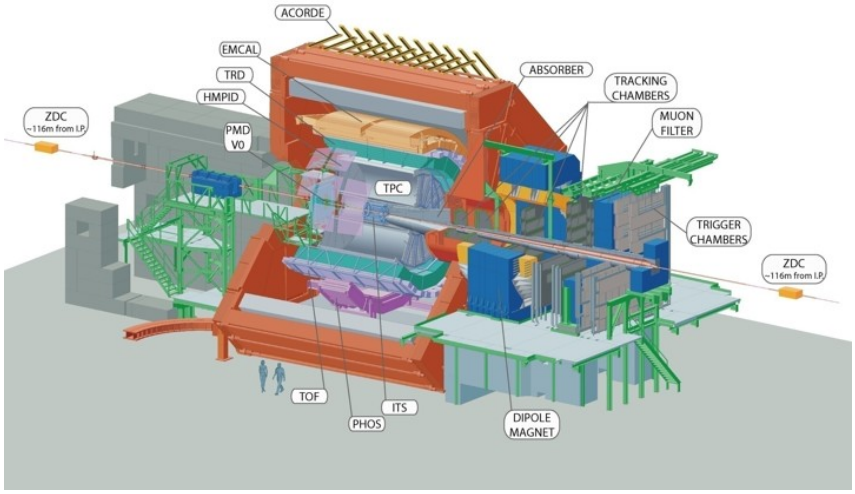

Figure 2.1: Schematic overview of the ALICE detector [20].

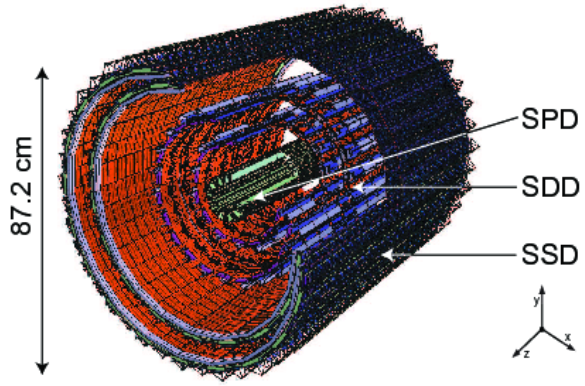

Figure 2.2: Schematic overview of the Inner Tracking System with its different layers (SPD, SDD and SSD), see text for details [22].

implies that the ITS can distinguish between prompt particles (particles that originate from the primary vertex, i.e. the collision point) and feed-down particles (particles that originate from a secondary vertex, i.e. a vertex that is not at the collision point) [21].

In figure 2.2 a schematic overview of the ITS is depicted. The ITS detector consists of six cylindrical layers of silicon detector. The cylinders are about a meter long and have radii from 3.9 cm up to 43.6 cm. A silicon detector works by doping (i.e. introduce impurities to a very pure semi-conductor) a strip of silicon. This process turns the silicon strips into small diodes. When charged particle pass through the strip, a small ionization current will be induced. This current can be measured. By adding a lot of strips together, one can get a detailed description of the path of a charged particle.

In the ITS three different types of silicon detectors are used. The two innermost layers are formed by Silicon Pixel Detectors (SPD). The middle layers are formed by Silicon Drift Detectors (SDD) and the two outermost layers are made of Silicon Strip Detectors (SSD). The choice for these types is mainly based on the requirements for the resolution of the impact parameter and the expected particle density that passes through the layers.

2.1.2 Time Projection Chamber

The Time Projection Chamber (TPC) is the main tracking detector in the ALICE central barrel. A sketch of the TPC is depicted in figure 2.3. The TPC subdetector consists of a large volume of 88 m^3 filled with a 90% Ne, 10% CO_2 gas mixture. The TPC makes use of the fact that charged particles traveling through the TPC will ionize particles in the gas. The freed electrons will then be accelerated by an electric field to the end of the cylinder. By detecting these electrons, the TPC can reconstruct the tracks of the particles moving through the gas. The track reconstruction and separation is the most important capability of the TPC. However, the TPC is also able to determine the momenta of the particles from the reconstructed tracks. In addition, the TPC provides the first step of particle identification by measuring the energy loss of the particles at their respective momenta, since the energy loss as a function of momentum is characteristic for each particle, as shown in figure 2.4.

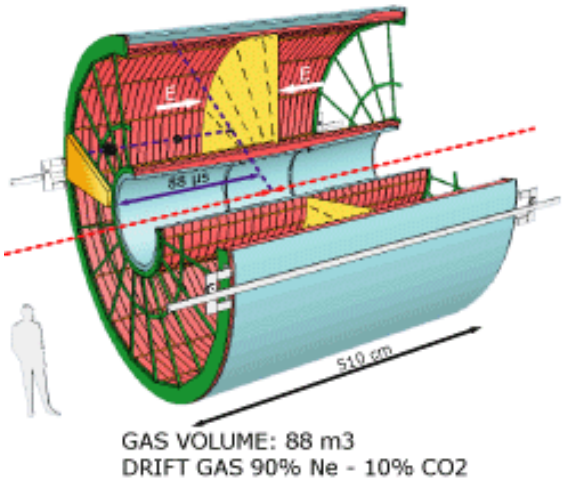

Figure 2.3: Schematic overview of the Time-Projection Chamber [21].

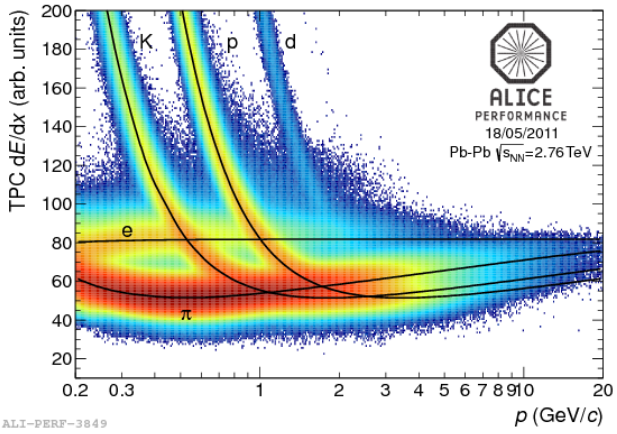

Figure 2.4: Measured specific ionisation energy loss, dE/dx, as a function of momentum, p, in the TPC for different particles [24].

2.1.3 Time of Flight detector

The Time of Flight (TOF) detector, depicted in figure 2.5, consists of an array of 1638 Multi-gap Resistive Plate Chambers (MRPCs) arranged in a cylindrical configuration at a radius of 370 cm up to 399 cm covering an area of 160 m^2 in total. The MRPCs consist of a stack of resisting glass plates. Just like in the TPC, the charged particles will ionize the gas in between. A high electric field amplifies this ionization by an electron avalanche. The avalanche development is stopped and measured at the resistive plates, while the signal moves through the glass plates. The TOF measures the time that the particle needs to travel from its vertex to the TOF with a precision greater than 10 ps [20]. The time measurement in the TOF together with momentum and the track length can be used for the particle identification for intermediate momenta, as shown in figure 2.6.

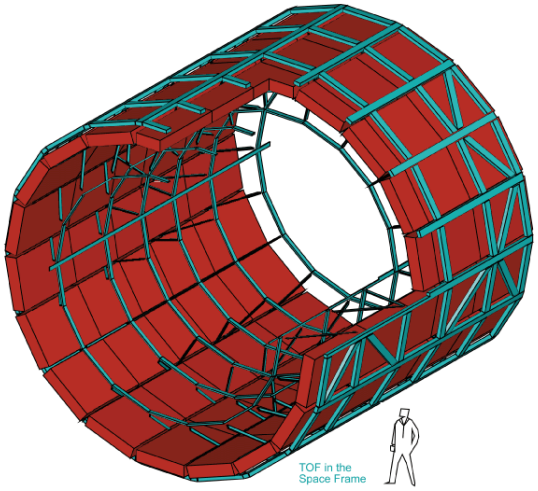

Figure 2.5: Schematic overview of the Time of Flight subdetector [21].

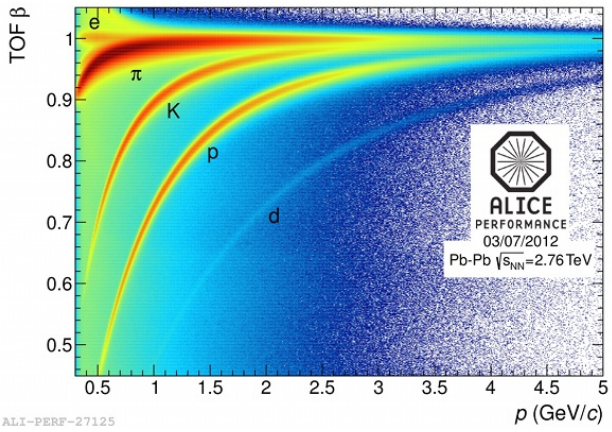

Figure 2.6: Particle identification in the TOF by measuring the time of flight and calculating from this the particle velocity $\beta = \frac{v}{c}$ as a function of momentum [23].

2.2 Analysis framework

For this thesis, I made use of a Monte-Carlo simulated data set. The data set consists of simulated data from proton-proton collisions in the ALICE experiment at 7 TeV. The actual collisions took place in 2010. The data set has been produced with the event generator PYTHIA. PYTHIA is a program that uses Monte-Carlo techniques to simulate particle collisions such as proton-proton collisions. For this, it uses the laws of physics that are provided by theory. A nice property of PYTHIA is that one can choose to 'force' a sample. Basically, this means that one can ask PYTHIA to generate a high branching ratio for a certain decay channel, while in nature this decay channel has a very low branching ratio. This allows us to study decay channels with low branching ratios more efficiently.
The analysis of the data set in this thesis is done within the AliRoot framework, which is an extension of the Root framework. Root is an analysis framework that is designed by Fons Rademakers and René Brun in 1995 and is written in the object oriented programming language C++. Root was developed at CERN and is also used by scientists in other branches of physics. Root is built in a layered class hierarchy with around 250 classes, which are grouped into different libraries [25]. Several classes have been used in this thesis. Most important for this thesis were the TH1 and TF1 class, which can be used to make histograms of data and fit them according to a certain distribution.
The AliRoot framework is based on Root, but developed for the ALICE detector. The most important aspect of the AliRoot is that it incorporates the ALICE detector. AliRoot can handle both real data and Monte-Carlo simulations. Furthermore, AliRoot can generate its own simulations using PYTHIA. In the further analysis of this data, AliRoot not only analyzes the simulated data set, but it also quantizes the response of the ALICE detector to the data. Therefore, the analysis of Monte-Carlo simulated data in the AliRoot framework will be closer to the actual measurement of data.

3 The Monte-Carlo data set and analysis method

All of the analysis has been done on the LHC10f7a data set. This is a charm forced MC anchored data set from CERN reproducing the 2010 ALICE p-p data [26]. A major advantage of this data set, is that the ratio of the D^{*+}-mesons coming from a B-meson to those coming from a charm quark is roughly 1:1. In contrast, in the universe this ratio is about 1:40 and in the Alice detector for Pb-Pb collisions at 2.76 TeV it is measured to be between 1:20 for low momenta and 1:10 for high momenta [27]. Since the ratio is 1:1 in the data set, the feed-down decay (from a B-meson) can be studied more effectively. The full data set consists of 25 million events (p-p collisions). For the study described in this thesis about 0.5 million events have been used.

3.1 The decay channel

As mentioned in the first chapter, the production of D^{*+}-mesons from charm and from beauty quark fragmentation is studied (equation 3). For the D^{*+}-mesons, the following decay channel has been studied[4] [17]:

$$D^{*+} \to D^0 + \pi_s^+ \qquad BR = (67.7 \pm 0.5)\% \tag{5}$$

$$D^0 \to K^- + \pi^+ \qquad BR = (3.88 \pm 0.05)\%, \tag{6}$$

where π_s^+ is called the soft pion, because of its low momentum. In this specific MC data set, the branching ratio of the $D^0 \to K^- + \pi^+$ has been increased to 8.09% [26].

3.2 Analysis of the data sample

As a basis, a so called CERN approved code [28] has been used. All results presented in this thesis have been obtained by adding extra code and applying it to the afore mentioned data set.
The analysis has been done on a Monte Carlo data set, which has as advantage that the full decay process is saved. This means that one can ask for the exact momentum, identity and the location of the vertex of origin of every particle. In addition one can ask for the mother, grandmother, daughters etc. of the particle. In particular, one can make a distinction between the particles D^{*+}-mesons coming from charm quarks and those coming from B-mesons. Whenever plots of the signal are presented, it has been verified by particle identification in the Monte-Carlo sample that only the signal (i.e. data from the specified decay channels) is shown in the plot. The presented properties, like momentum, invariant mass and impact parameter, are the properties as it would be measured by the detector.
The real data, however, is not that easy to analyze, since one can only ask for properties like momentum, identity, location of the vertex of origin with an uncertainty. Furthermore, one can only see the particles, which are really measured. There will always be particles that will not be detected by the detector, or which will only be detected a few times. If there are not enough detections of a particle, the uncertainty in reconstruction gets larger.
In order to get a better comparison with real data, several cuts on the MC-sample have been applied. A cut on the pseudo rapidity $|\eta| < 0.9$ has been applied. This basically means that only particles flying with a polar angle $45° < \theta < 135°$ are considered. In addition, the standard cuts, ITS and TPC refit, on the quality of the reconstruction of the track in the ITS and TPC are used. The quality is determined by the number of detections in the detector

[4] By replacing all particles by their anti-particle, one also gets an allowed decay channel. In the rest of the thesis, when a certain decay is mentioned, a combination of the decay and its 'anti-decay' is meant. Hence, for all of the results in the thesis both the decay and anti-decay have been studied without making a distinction between those two.

and the amount of kinks in the track. The cut is based on the χ^2_{red} of the reconstruction of the track.
Also comparison of the feed-down signal with the background has been done. The candidates are found by analyzing the data of the MC data set in the AliRoot framework, as if it were real data. This will yield only a small signal and a lot of combinatorial background, since the detector will analyze every possible combination of a kaon and 2 pions as a possible D^{*+}-meson. The small signal will be comparable to statistical fluctuations and negligible compared to the combinatorial background. Therefore, the signal cannot be analyzed directly. In order to analyze the signal, cuts on the data have to be applied. Cuts are designed to cut out a lot of combinatorial background, but only a very small fraction of the signal. In previous research cuts on event selection, track quality (this includes the pseudo-rapidity, ITS and TPC refit cuts), particle identification and 16 topological cuts have been designed[5] [3]. For optimizing those cuts the statistical significance has been introduced:

$$S_g = \frac{S}{\sqrt{S+B}}. \tag{7}$$

Here, S and B are the number of entries of the signal and background respectively close to the signal range.[6] The statistical significance is a measure for how many times the signal S is larger than the fluctuations of the signal and the background $\sqrt{S+B}$. Optimizing the statistical significance[7] results in a better visible signal and improves the quality of the further analysis. For this thesis, standard cuts on the candidates used in [28] have been used. The background used in this thesis is the background that is left after the cuts have been applied.

3.3 Invariant mass reconstruction

In order to measure the D^{*+}-mesons in the real data, one looks at the invariant mass of the particle. The invariant mass is a Lorentz invariant characteristic of the particle's total energy and momentum. The D^{*+}-mesons have decayed before they reach the detector, so their invariant mass cannot be calculated directly. The invariant mass can, however, be reconstructed by looking at the decay products of the D^{*+}-meson. Looking at the decay channel specified in equation 5, one sees that the measured decay products are pions and kaons. Now one can use the invariant mass formula given by:

$$M = \sqrt{E^2 - |\overrightarrow{p}|^2}. \tag{8}$$

However, neither the energy nor the momentum of the D^{*+}-meson is known. Hence, the formula has to be adapted slightly to reconstruct the D^{*+} invariant mass from the kaons and pions:

$$M = \sqrt{\left(\sum_i E_i\right)^2 - \left|\sum_i \overrightarrow{p_i}\right|^2}. \tag{9}$$

Here, the sum is over all decay products of the particle. For the D^{*+}-meson and the afore mentioned decay channel this formula becomes:

$$M(D^{*+}) = \sqrt{(E_K + E_{\pi_1} + E_{\pi_2})^2 - |\overrightarrow{p_K} + \overrightarrow{p_{\pi_1}} + \overrightarrow{p_{\pi_2}}|^2}. \tag{10}$$

It is convenient to look at the invariant mass difference defined as:

$$\Delta M = M(D^{*+}) - M(D^0), \tag{11}$$

[5] A detailed description of all the cuts can be found in [3]
[6] A commonly used value in real data is $\pm 3\sigma$ around the mean of the signal peak, but other ranges can be used as well.
[7] A value of $S_g = 3$ is commonly taken as required minimum for a signal to be significant.

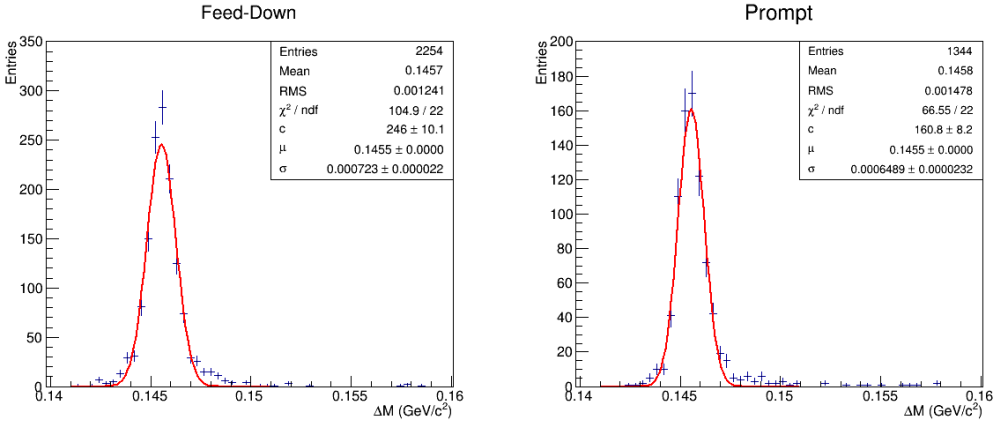

Figure 3.1: ΔM of the feed-down (left) and prompt (right) D^{*+} signal as measured by the ALICE detector. Gaussian fits have been applied to the data.

where

$$M(D^0) = \sqrt{(E_K + E_{\pi_1})^2 - |\overrightarrow{p_K} + \overrightarrow{p_{\pi_1}}|^2}. \tag{12}$$

Since the detector is not capable of measuring the energy of the detected particle, one has to calculate it. In order to do this, one has to make a mass assumption. This means that one assumes that a detected particle is a certain particle and uses its known rest mass to calculate the energy by a rearrangement of equation 8:

$$E_i = \sqrt{M_i^2 + |\overrightarrow{p_i}|^2}, \tag{13}$$

where i can be any particle. In this case $i \in \{K, \pi_1, \pi_2\}$. When the detected particle is indeed the particle that was assumed, this will yield the correct value for the energy. When this is not the case, the calculated energy will be wrong. The particle identification in the detector helps finding the right mass assumptions. However, the particle identification is not 100% reliable. Therefore, there will always be some wrongly calculated invariant masses. By applying cuts on the invariant mass, one can cut out a lot of invariant masses that are calculated from wrong mass assumptions.

As a first study of the sample, the invariant mass of the D^{*+}-mesons is calculated and fitted according to a Gaussian function. For this, the sample has been divided in feed-down and prompt D^{*+}-mesons, as shown in figure 3.1. In this figure, the p_T integrated invariant mass is shown. To get a more detailed study, one could look at the invariant mass of the D^{*+}-mesons for different transverse momenta (the momentum perpendicular to the beamline) of the D^{*+}-meson. In order to do this the data has been split in p_T bins of the D^{*+}-meson. The bins $[1.0, 3.0]$ GeV/c, $[3.0, 5.0]$ GeV/c, $[5.0, 8.0]$ GeV/c and $[8.0, 16.0]$ GeV/c have been used. By doing this, one can make plots like in figure 3.1 for every p_T bin. These plots are very similar to figure 3.1 and can be found in appendix A. One could also look at the invariant mass difference as a function of the transverse momentum of the D^{*+}-meson for feed-down and prompt D^{*+}-mesons. This is shown in figure 3.2. Here, the points are plotted along the x-axis on the average transverse momentum of their respective p_T bin.

We find for the invariant mass difference of the D^{*+}-meson: $\Delta M = (145.5 \pm 0.5)$ MeV/c^2, which is just above the rest mass of a charged pion ($m_{\pi^\pm} = (139.57018 \pm 0.00035)$ MeV/c^2 [17]). This is where it is expected to be, since the invariant mass difference is expected to be equal to the sum of the rest mass energy of a charged pion and some kinetic energy. Figure 3.1 and figure 3.2 show that there is no significant difference in the invariant mass difference between feed-down and prompt D^{*+}-mesons. Furthermore, the standard-deviation of the Gaussian gets slightly smaller for higher transverse momenta of the D^{*+}-meson.

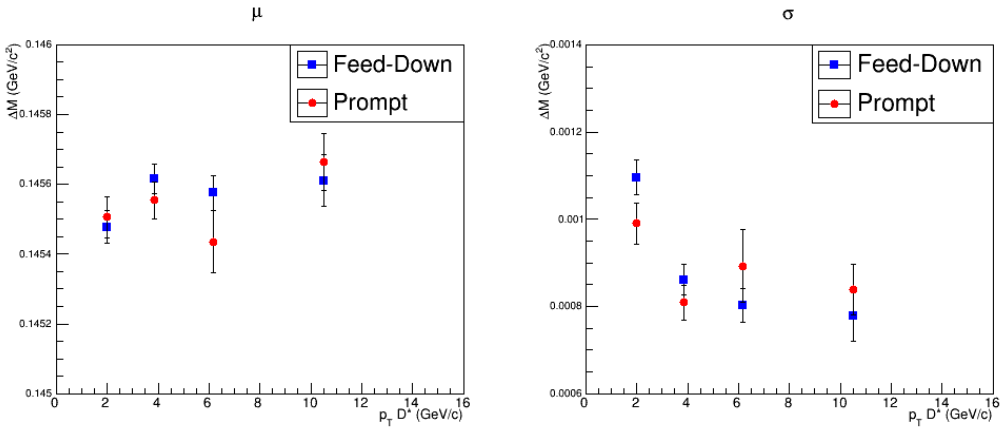

Figure 3.2: The invariant mass difference, ΔM, as a function of the transverse momentum, p_T, for feed-down (blue symbols) and prompt (red symbols) D^{*+}-mesons of the signal as measured by the ALICE detector. Left: mean, μ, of the Gaussian peak. Right: width, σ, of the Gaussian peak.

3.4 Transverse momentum distributions of the D^{*+} and B-mesons

Next, we study the momentum distributions of the particles. Most interesting in the scope of this thesis is the relation between the momentum distribution of the B-mesons and the momentum distribution of the D^{*+}-mesons, since the motivation for this research is to cut out D^{*+}-mesons from the data in order to study the properties of the B-mesons. The momentum distribution of the D^{*+}-meson is shown in figure 3.3. The momentum distributions of the B-mesons separated in p_T bins of the D^{*+}-meson can be found in figure 3.4. Furthermore, the transverse momentum of the B-meson is shown as a function of the transverse momentum of the D^{*+}-meson in figure 3.5. In this figure, all B-mesons that decay into a D^{*+}-meson have been taken into account. There are different kinds of B-mesons that decay into a D^{*+}-meson. In this sample about 85% of all feed-down D^{*+}-mesons comes from a B^0 decay and 15% from decays of other B-mesons (this can be a $B^{\pm}$-meson but also a strange or charmed B-mesons or an excited B-meson). The momentum distributions of the kaons pions and D^0-mesons can be found in appendix B.

From figure 3.4 and 3.5, we can conclude that there is a strong correlation between the transverse momentum of the D^{*+}-meson and the transverse momentum of the B-mesons. A large B-meson with a high transverse momentum decays into a D^{*+}-meson with a high transverse momentum.

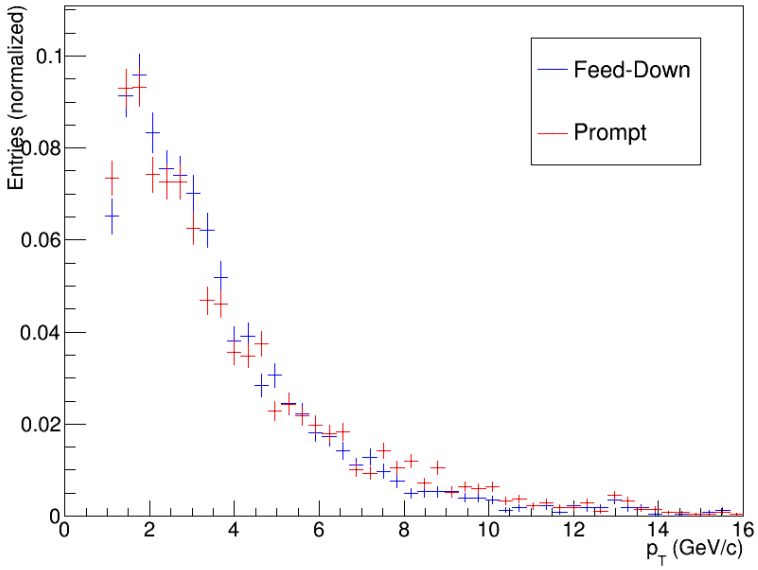

Figure 3.3: Normalized transverse momentum distributions of feed-down (blue symbols) and prompt (red symbols) D^{*+}-mesons.

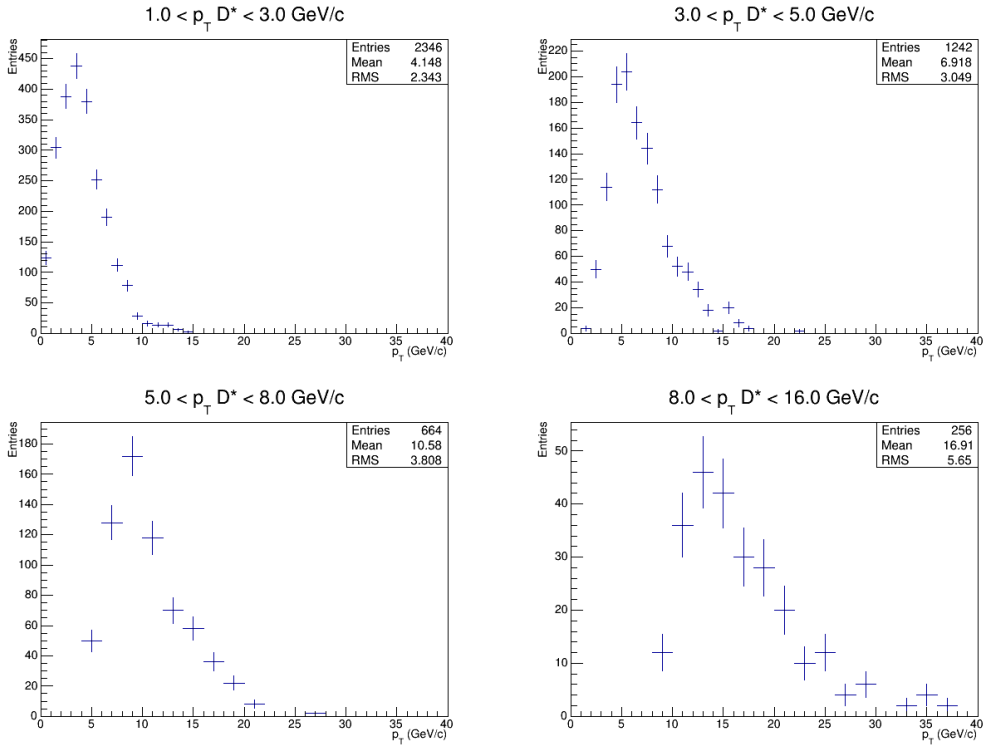

Figure 3.4: Transverse momentum distributions of the B-mesons in p_T bins of the D^{*+}-meson.

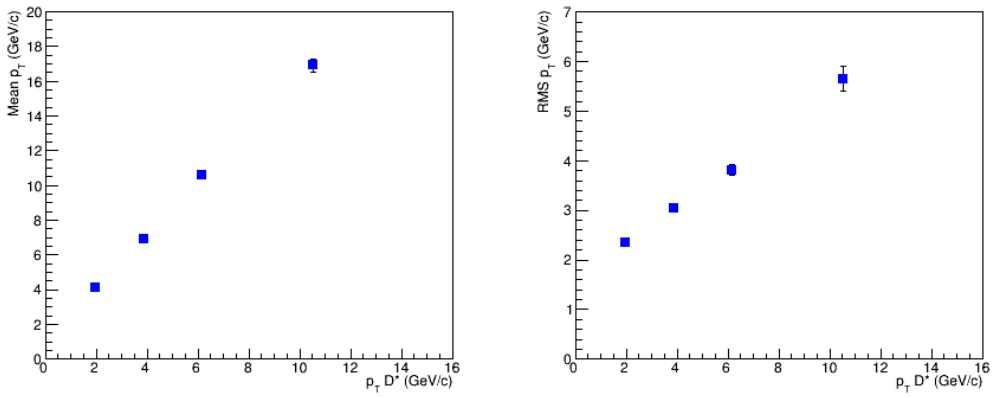

Figure 3.5: Mean (left) and RMS (right) of the transverse momentum distributions of the B-mesons in p_T bins of the D^{*+}-meson.

4 Cuts on impact parameter

In order to cut on the impact parameter, the error in the position determination of the detector should not be larger than the impact parameter itself. As already mentioned in section 2.2.1, the detector has an accuracy of 100 μm for the primary vertex. As mentioned in section 1.6, the B-meson flies for about 500 μm. This implies that the error is in the same order of magnitude as the difference in impact parameter. Hence, one expects that the difference can be measured, but only with enough statistics to make the difference in the distributions of the impact parameter visible. For this research the error in the the position determination has been investigated. We found for the kaons and pions from D^0 and soft pions an error that is larger than 100 μm. However, it is of the same order of magnitude. Hence, the conclusion that we should be able to see the difference with enough statistics is still valid. An overview of the results of this studies and a brief discussion can be found in appendix C.

4.1 Impact parameter distributions of the D^{*+} and its daughters

After these preparations, we can start to look at the impact parameter of the kaon and pion from D^0 and the soft pion.[8] The results are shown in figure 4.1. The distributions of the impact parameter hint to an exponentially modified gaussian distribution. This distribution has, therefore, been used to fit the histograms. With the fits of the histograms we are able to calculate a ratio:

$$ratio = \frac{\text{number of feed-down mesons}}{\text{number of (feed-down + prompt) mesons}}, \tag{14}$$

where the mesons are kaons and pions from D^0 and the soft pions. The results for this ratios are shown in figure 4.2.
Next, the impact parameter of the D^{*+} and the D^0-meson is studied, as shown in figure 4.3. Although, we cannot directly measure these particles in the real data, looking at the distribution of the impact parameter of these particles is interesting, because we are looking for the difference in impact parameter of the D^{*+}-meson. These histograms have also been fitted, and from the fits we calculate again a ratio, as shown in figure 4.4.
To get a more detailed look into the distribution of the impact parameter, we will again divide the sample into p_T bins of the D^{*+}-meson. With the impact parameter distributions in these bins we can do the same analysis as with the p_T integrated distribution. The histograms of the impact parameter are shown in figure 4.5 for the pion from D^0, figure 4.6 for the kaon from D^0, figure 4.7 for the soft pion, figure 4.8 for the D^{*+}-meson and figure 4.9 for the D^0-meson. Again the ratios are studied. These are shown in figure 4.10 for the pion and kaon from D^0 and the soft pion, figure 4.11 for the D^{*+}-meson and figure 4.12 for the D^0-meson.
Lastly, the average impact parameter as a function of the D^{*+}-meson is studied. This is shown in figure 4.13 for the pion and kaon from D^0 and the soft pion and in figure 4.14 for the D^{*+} and D^0-mesons. In these figures, the background is shown as well.
We see a slight decay of the impact parameter with increasing p_T of the D^{*+}-meson. This decay is most visible for the pion and kaon from D^0 and the soft pion, which have a significantly higher impact parameter than the D^{*+} and D^0-meson. This result might look counterintuitive, since one expects particles with higher momentum (hence, higher velocity) to fly further before they decay. This should yield a higher impact parameter for faster particles. However, the particles are also affected by the magnetic field in the detector. The

[8] In order to get enough statistics the histograms shown in this chapter have been obtained by J. van der Maarel (Ph.D. student in our group) by running a larger sample of the same data set (LHC10f7a) on the ALICE grid.

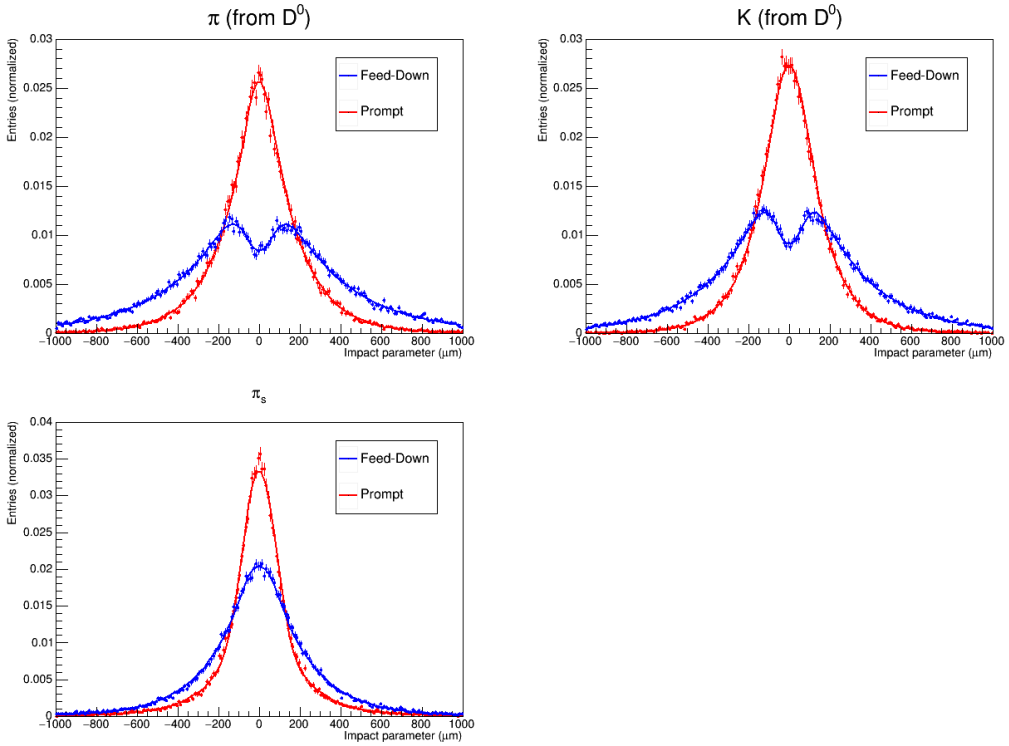

Figure 4.1: Impact parameter distributions of the feed-down (blue) and prompt (red) pions (top left) and kaons (top right) from D^0 decays and soft pions (bottom left) with exponentially modified Gaussian fits.

magnetic field curves the tracks of the particles. The curvature is stronger for particles with lower momentum. Because of this curvature, the tangent line of the track at the decay vertex will be more tilted. Since the impact parameter of the particle is defined as the distance of closest approach from this tangent line to the primary vertex, this effect will increase the impact parameter more for particles with lower momentum. This effect is most visible for the pion and kaon from D^0 and soft pion, since they are at the end of the decay chain. Therefore, their tracks have been affected the most by the magnetic field.
The other results (figure 4.1 till 4.12) will be discussed in the next section.

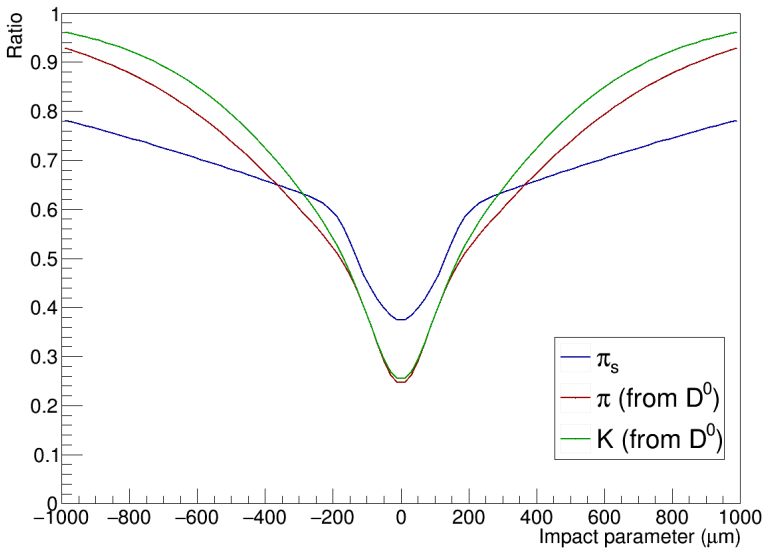

Figure 4.2: Ratio FeedDown/(FeedDown+Prompt) of the fits of the impact parameter for the feed-down and prompt pion (red) and kaon (green) from D^0 decays and soft pions (blue).

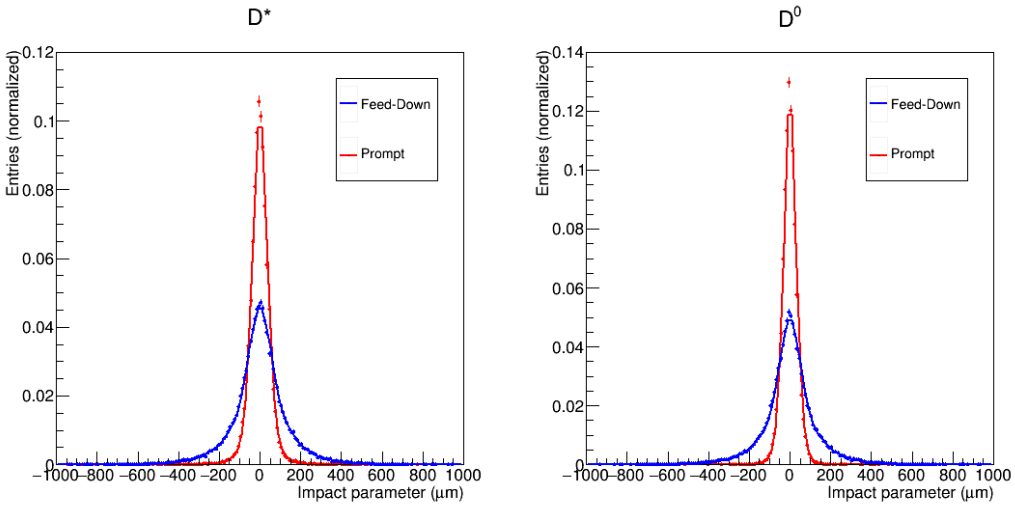

Figure 4.3: Impact parameter distributions of the feed-down (blue) and prompt (red) D^{*+} (left) and D^0-mesons (right) with exponentially modified Gaussian fits.

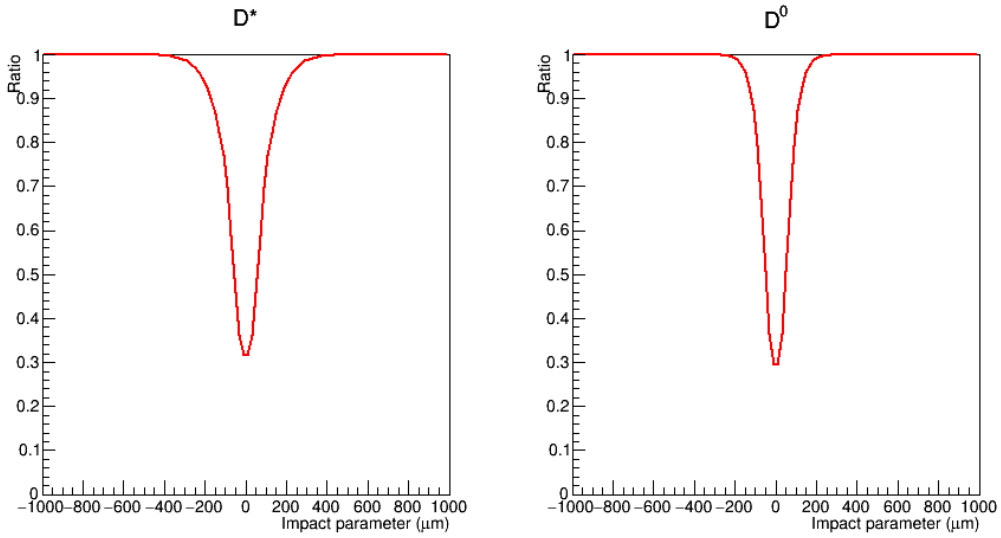

Figure 4.4: Ratio FeedDown/(FeedDown+Prompt) of the fits of the impact parameter for the feed-down and prompt D^{*+} (left) and D^0-mesons (right).

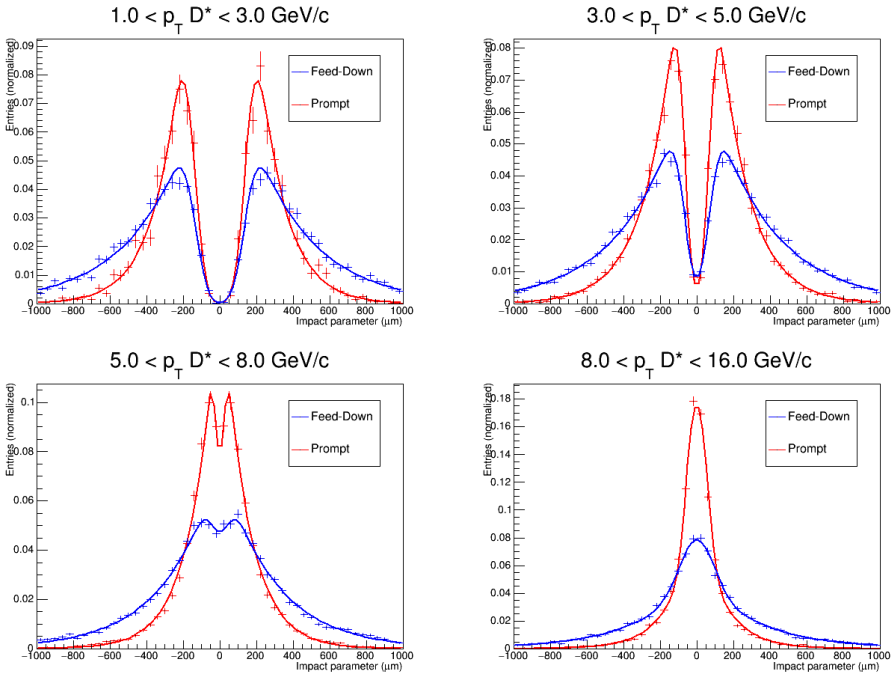

Figure 4.5: Impact parameter distributions of the feed-down (blue) and prompt (red) pions from D^0 decays in p_T bins of the D^{*+}-meson with exponentially modified Gaussian fits.

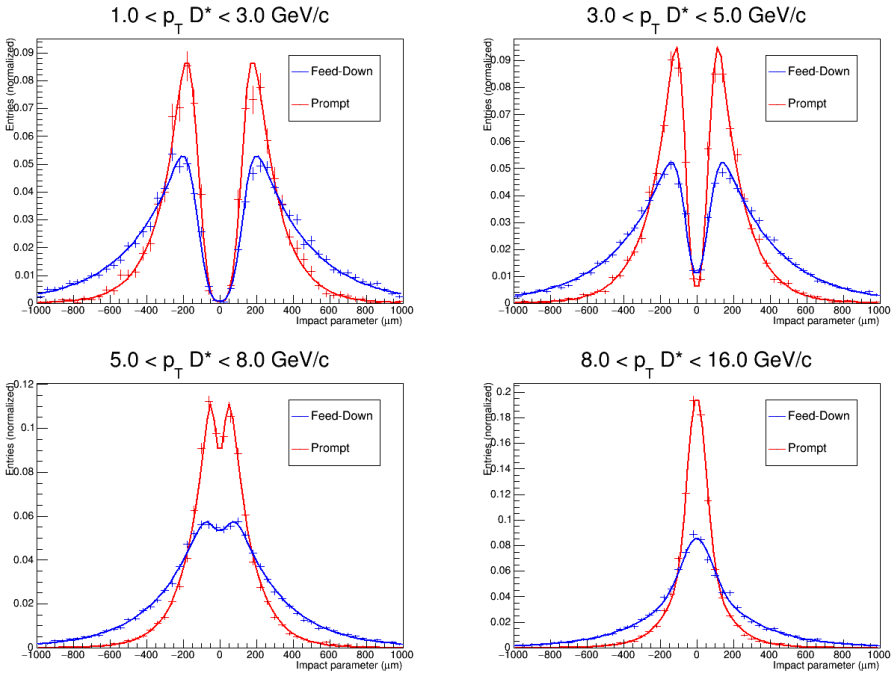

Figure 4.6: Impact parameter distributions of the feed-down (blue) and prompt (red) kaons from D^0 decays in p_T bins of the D^{*+}-meson with exponentially modified Gaussian fits.

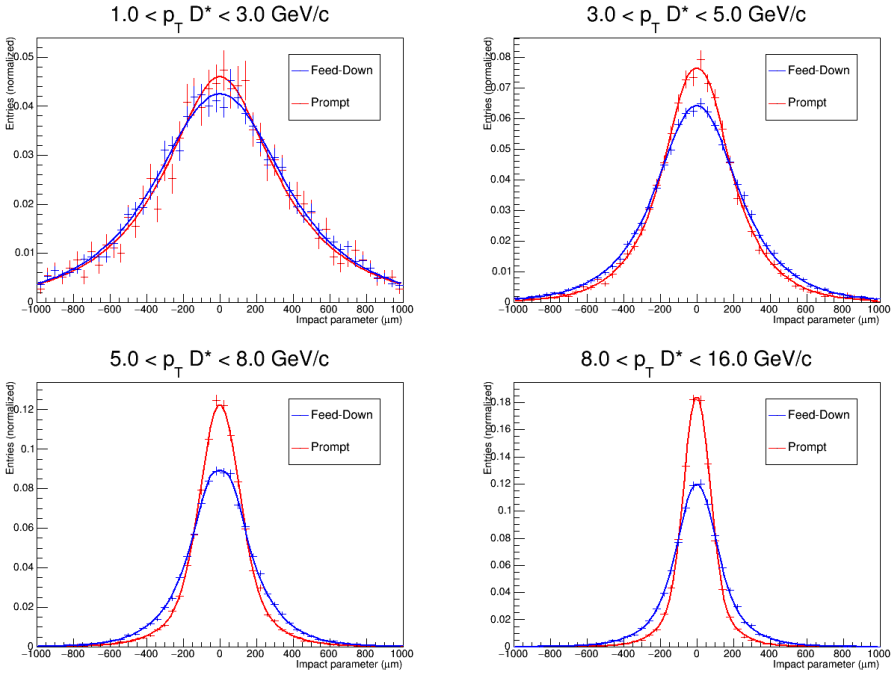

Figure 4.7: Impact parameter distributions of the feed-down (blue) and prompt (red) soft pions in p_T bins of the D^{*+}-meson with exponentially modified Gaussian fits.

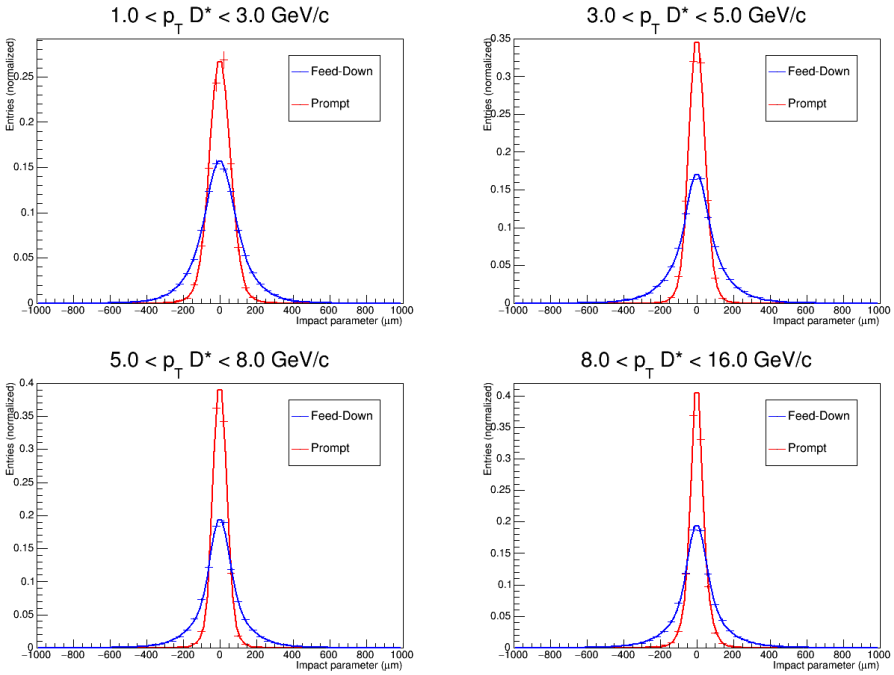

Figure 4.8: Impact parameter distributions of the feed-down (blue) and prompt (red) D^{*+}-mesons in p_T bins of the D^{*+}-meson with exponentially modified Gaussian fits.

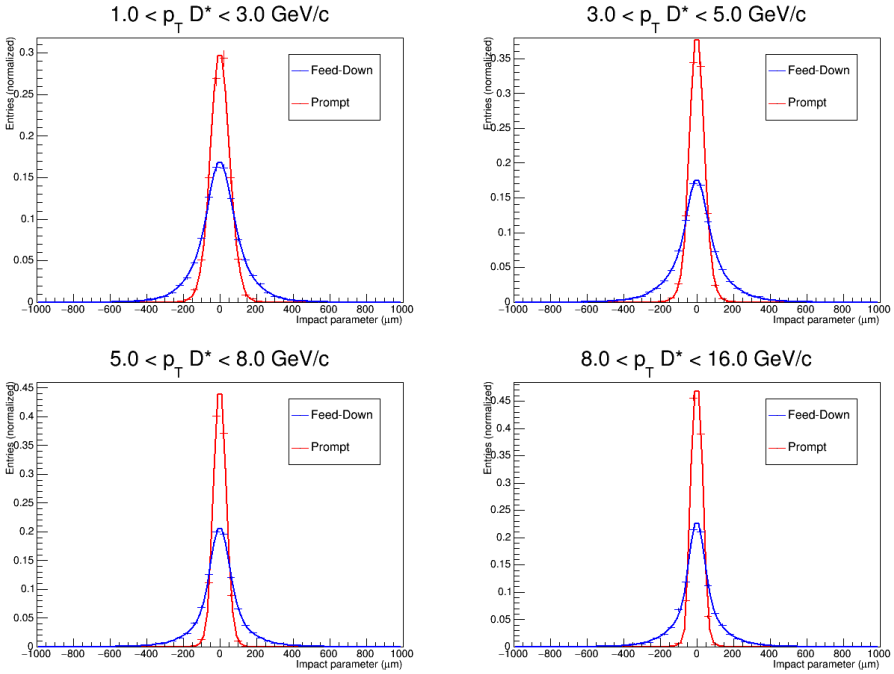

Figure 4.9: Impact parameter distributions of the feed-down (blue) and prompt (red) D^0-mesons in p_T bins of the D^{*+}-meson with exponentially modified Gaussian fits.

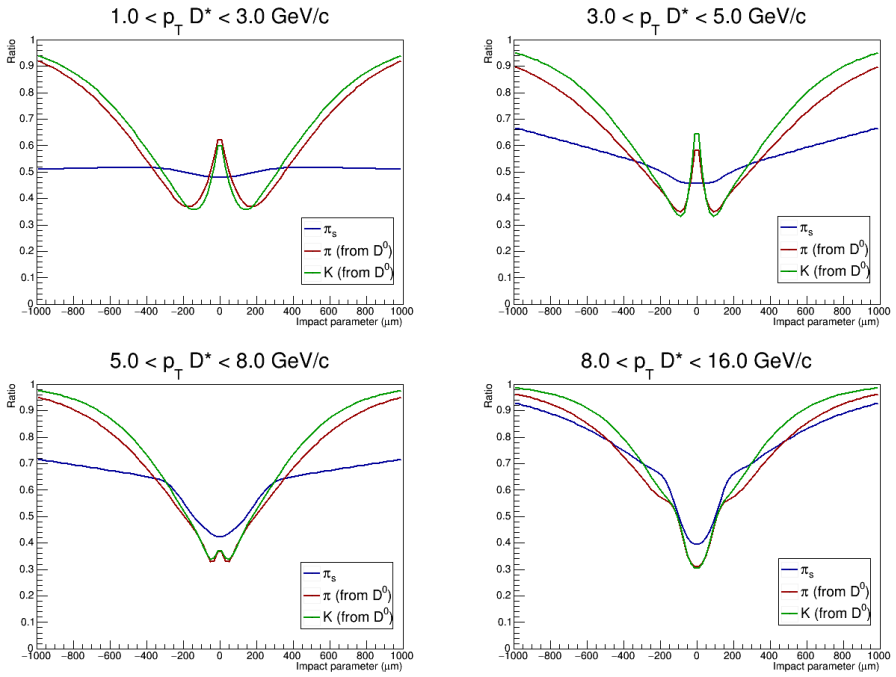

Figure 4.10: Ratio FeedDown/(FeedDown+Prompt) of the fits of the impact parameter for the feed-down and prompt pion (red) and kaon (green) from D^0 decays and soft pion (blue) in p_T bins of the D^{*+}-meson.

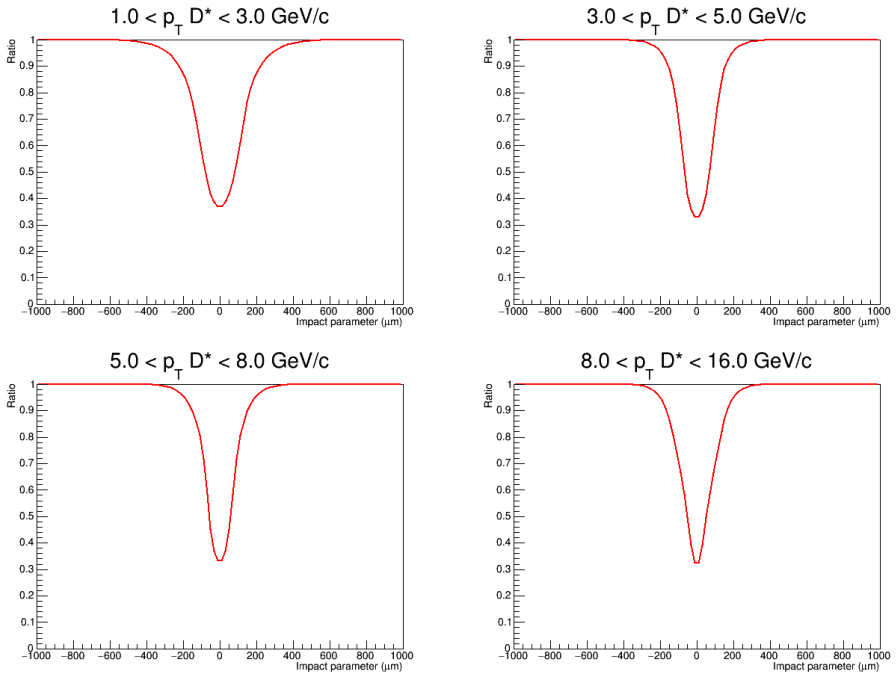

Figure 4.11: Ratio FeedDown/(FeedDown+Prompt) of the fits of the impact parameter for the feed-down and prompt D^{*+}-meson in p_T bins of the D^{*+}-meson.

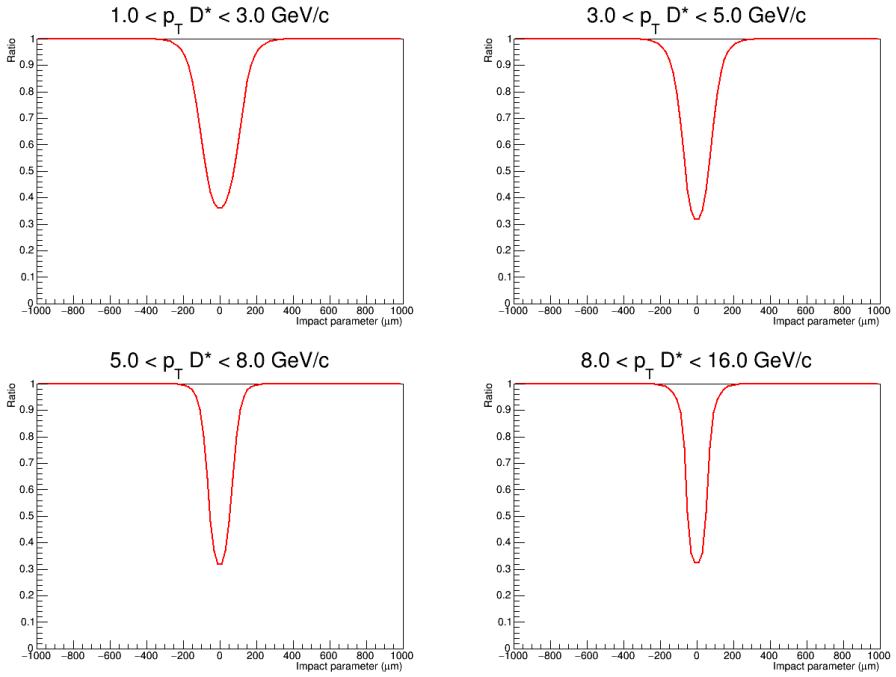

Figure 4.12: Ratio FeedDown/(FeedDown+prompt) of the fits of the impact parameter for the feed-down and prompt D^0-meson in p_T bins of the D^{*+}-meson.

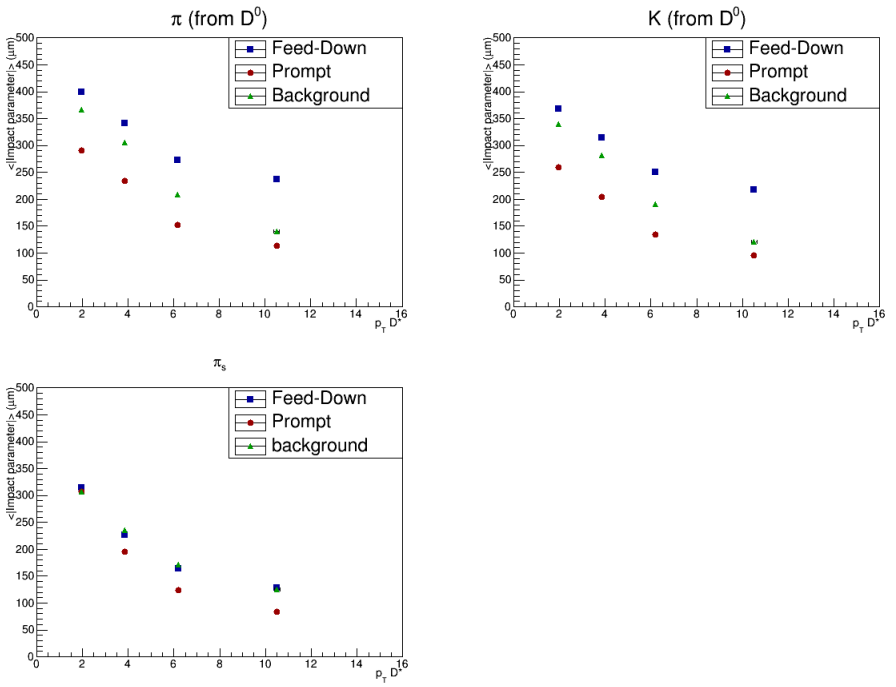

Figure 4.13: Average impact parameter distributions for the feed-down (blue), prompt (red) and background (green) pion (top left) and kaon (top right) from D^0 decays and soft pion (bottom left) as a function of the p_T of the D^{*+}-meson.

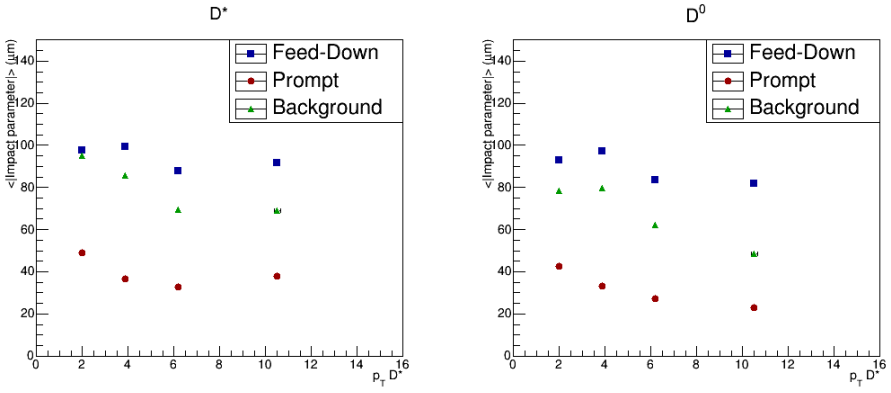

Figure 4.14: Average impact parameter distributions for the feed-down (blue), prompt (red) and background (green) D^{*+} (left) and D^0 (right) as a function of the p_T of the D^{*+}-meson.

4.2 Purity of the sample after applied cuts

The figures with the ratios in the previous 2 subsections showed a clear increase of the ratio with increasing impact parameter. This shows that cuts may be applied on the impact parameter to increase the fraction of the feed-down D^{*+}-meson. I have chosen to apply cuts on the impact parameter of the pion and kaon from D^0 decays and the soft pion, since these particles will actually be measured in real data. Therefore, one can directly cut on these particles' impact parameter without doing any further reconstruction. Secondly, I have chosen to take the same cut value for all three particles. This is done, because in real data the particles are not always identified correctly. A third argument for this last choice is that the ratio's of the kaon and the pion from D^0 decays are very similar, as can be seen in figure 4.2 and 4.10. As cut values for the Impact parameter I have chosen:

- |Impact parameter| > 400 μm
- |Impact parameter| > 600 μm
- |Impact parameter| > 800 μm

As can be seen in figures from the previous section |Impact parameter| $= 200$ μm is around the point, where the fraction of feed-down D^{*+}-mesons gets larger than the fraction prompt D^{*+}-mesons (i.e. the ratio gets larger than 0.5) and |Impact parameter| $= 1000$ μm is around the point, where almost all prompt and feed-down D^{*+}-mesons that follow the decay channel of interest are gone.
After applying these cuts one can look at the purity of the sample, which is defined as the ratio of the feed-down with respect to the prompt D^{*+}-mesons:

$$purity = \frac{\text{number of feed-down } D^{*+}\text{-mesons}}{\text{number of (feed-down + prompt) } D^{*+}\text{-mesons}}. \tag{15}$$

In addition, I will look at the purity with respect to the background:

$$purity_{Bck} = \frac{\text{number of feed-down } D^{*+}\text{-mesons}}{\text{number of (feed-down + background) } D^{*+}\text{-mesons}}. \tag{16}$$

The purities are shown in figure 4.15 and figure 4.16. The ratio of the remaining feed-down with respect to the number of feed-down D^{*+}-mesons before cuts were applied is shown in figure 4.17. The purities with their statistical significance and the ratio of remaining feed-down D^{*+}-mesons are summarized in table 1 and discussed in the next section.

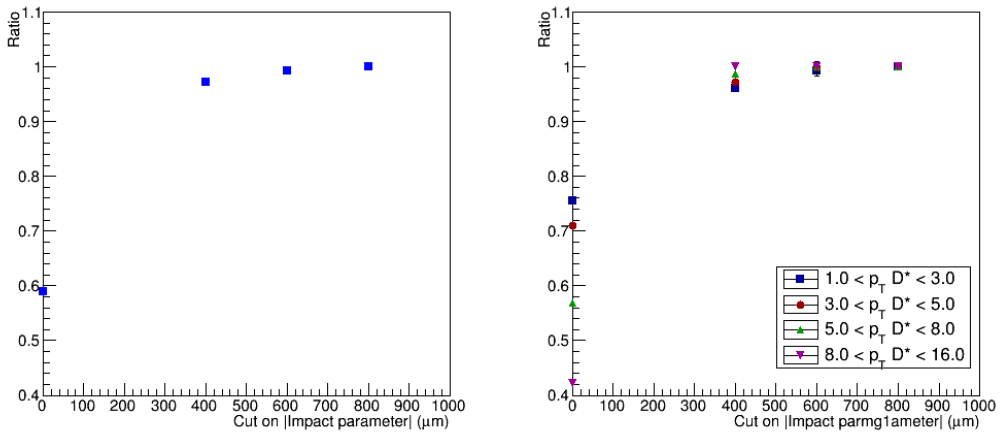

Figure 4.15: Purity, $\frac{\text{feed-down}}{\text{feed-down + prompt}}$, of the sample for the different cuts. Left: the p_T integrated signal. Right: The signal in p_T bins of the D^{*+}-meson.

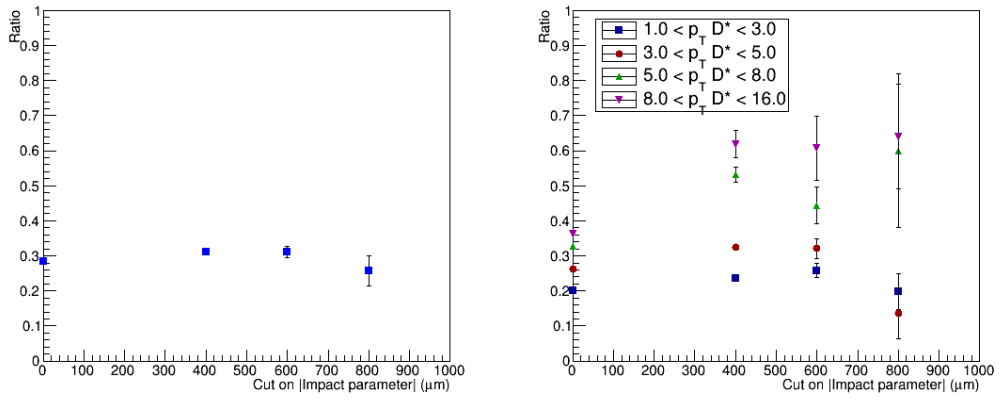

Figure 4.16: Purity, $\frac{\text{feed-down}}{\text{feed-down + background}}$ of the sample with respect to the background for the different cuts. Left: the p_T integrated signal. Right: The signal in p_T bins of the D^{*+}-meson.

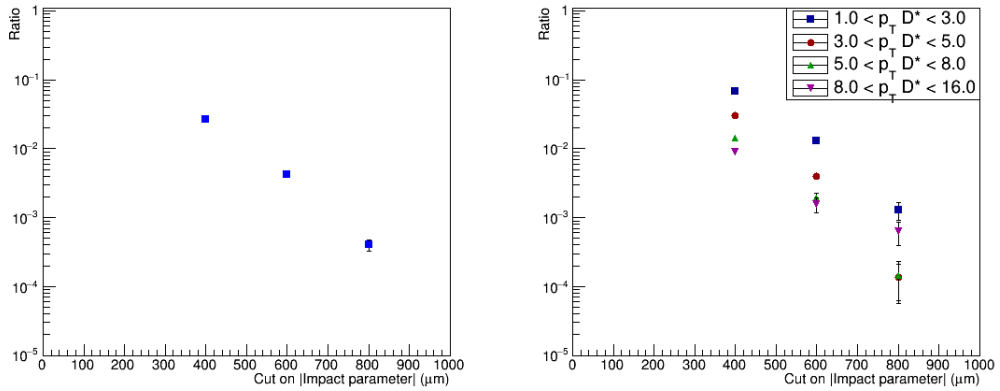

Figure 4.17: Ratio of remaining feed-down D^{*+}-mesons of the sample for the different cuts. If no cuts on impact parameter were applied, the ratio would be 1. Left: the p_T integrated signal. Right: The signal in p_T bins of the D^{*+}-meson.

Next, the invariant mass difference peak of the candidates, the signal and the feed-down and prompt D^{*+}-mesons, is studied. This study is done, because the invariant mass difference peak identifies the D^{*+}-meson in real data. The invariant mass difference peaks for the different cuts are shown in figure 4.18.
This figure shows that the higher the cut on impact parameter is, the higher the fraction of D^{*+}-mesons in the signal gets. This happens for the whole width of the signal's ΔM peak.

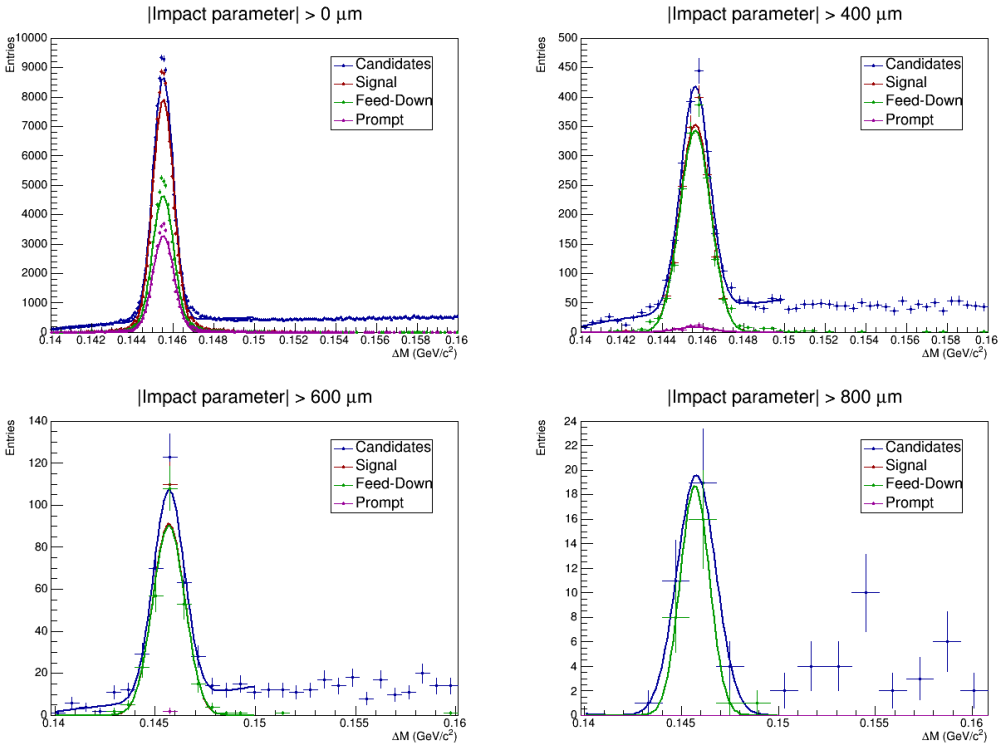

Figure 4.18: $\Delta M = M(D^{*+}) - M(D^0)$ distributions of the candidates (blue), the signal (red) and the feed-down (green) and prompt (magenta) D^{*+}-mesons for the different cuts on impact parameter with Gaussian fits. Note: in the 2 bottom figures the prompt distributions have not been fitted due to low statistics. Also, the fits of the signal are not shown in the bottom figures, since they are the same as the feed-down fits.

5 Discussion and Conclusions

The possibility for separation of the feed-down D^{*+}-meson from the prompt D^{*+}-meson has been investigated. The results in section 4.1 showed that such a separation is possible on the basis of the impact parameter of the decay products of the D^{*+}-meson (kaons and pions). I have chosen to cut the impact parameter on |Impact parameter| > 400 μm, |Impact parameter| > 600 μm and |Impact parameter| > 800 μm. The results for these cuts are shown in table 1 and in figure 4.15 till 4.18 in the previous section.
Table 1 shows that the purity for a cut on 800 μm removes all the prompt D^{*+}-mesons from the sample. For high transverse momentum of the D^{*+}-meson, an even lower cut can be applied (400 μm for $8 < p_T < 16$ GeV/c and 600 μm for $5 < p_T < 8$ GeV/c) to remove all the D^{*+}-mesons from the sample. A downside of these cuts is that the statistical significance gets lower for higher cuts. For the highest cut it even get below 3 for some p_T bins. This means that the found signal of feed-down D^{*+}-mesons becomes comparable with the statistical fluctuations of the feed-down and prompt D^{*+}-mesons together. Therefore, these results are not statistically significant.
In the next two columns of table 1, a comparison with the combinatorial background has been made. Most important for the results in this comparison is that $Purity_{Bck}$ does not get significantly lower for the applied cuts. Other cuts have been designed to cut out combinatorial background, as discussed in section 3.2. It is important, however, that the cuts on impact parameter do not increase the background ratio again. Fortunately, this is not the case, as shown in table 1. However, this conclusion cannot be drawn for the highest cut (800 μm), since the statistical significance of the result gets too low for this cut.
As a last column the percentage of remaining feed-down has been added. The loss of feed-down D^{*+}-mesons, because of the cuts, is high. This could be expected, since the cuts are applied on the tail of the distributions shown in section 4.1. It implies, however, that a lot of data is needed, for a study, where one wants to separate the feed-down and prompt D^{*+}-mesons on their impact parameter.

Table 1: The purities, remaining percentage and statistical significance for the different cuts and different p_T bins. Purity has been calculated with respect to the prompt D^{*+}-mesons ($Purity$) and with respect to the background D^{*+}-mesons ($Purity_{Bck}$).

Cut (μm)	$p_T(D^{*+})$ (GeV/c)	$Purity$	S_g	$Purity_{Bck}$	$S_{g,Bck}$	Remaining feed-down
No Cut	Integrated	59.0%	195.0 ± 0.6	28.4%	135.2 ± 0.5	100%
	1-3	75.5%	84.3 ± 0.6	20.1%	43.4 ± 0.4	100%
	3-5	70.9%	125.8 ± 0.6	26.3%	76.6 ± 0.5	100%
	5-8	56.9%	108.2 ± 0.6	32.8%	82.1 ± 0.5	100%
	8-16	42.2%	68.3 ± 0.5	36.2%	63.3 ± 0.5	100%
400	Integrated	97.1%	41.0 ± 0.5	31.1%	23.2 ± 0.5	2.68%
	1-3	96.0%	25.0 ± 0.5	23.5%	12.4 ± 0.4	6.92%
	3-5	97.1%	25.5 ± 0.5	32.5%	14.8 ± 0.5	3.00%
	5-8	98.7%	17.1 ± 0.5	53.1%	12.5 ± 0.6	1.44%
	8-16	100%	9.9 ± 0.5	61.9%	7.8 ± 0.6	0.896%
600	Integrated	99.3%	16.4 ± 0.5	31.0%	9.2 ± 0.5	0.420%
	1-3	99.2%	11.0 ± 0.5	25.8%	5.6 ± 0.5	1.30%
	3-5	98.9%	9.4 ± 0.5	32.1%	5.3 ± 0.5	0.399%
	5-8	100%	6.3 ± 0.5	44.4%	4.2 ± 0.5	0.195%
	8-16	100%	4.1 ± 0.5	60.7%	3.2 ± 0.6	0.154%
800	Integrated	100%	5.1 ± 0.5	25.7%	2.6 ± 0.5	0.0403%
	1-3	100%	3.5 ± 0.5	19.7%	1.5 ± 0.4	0.128%
	3-5	100%	1.7 ± 0.5	13.6%	0.6 ± 0.3	0.0134%
	5-8	100%	1.7 ± 0.5	60.0%	1.3 ± 0.6	0.0146%
	8-16	100%	2.6 ± 0.5	63.6%	2.1 ± 0.6	0.0633%

6 Outlook

6.1 Comparison with Pb-Pb data at 5.5 TeV

The studies in this thesis have been done on a MC data sample, that simulates the data of the 2010 p-p interactions at 7 TeV. However, an update plan to the ALICE detector has been made lately. In particular, the inner tracking system will be upgraded. Because of this upgrade, the position of the vertices can be reconstructed more accurately. Hence, we might get even better results in real data of Pb-Pb collisions at 5.5 TeV than in the studies performed in this thesis. To look into this I compared the resolution and the invariant mass reconstruction in my studies to those of a studies on a 5.5 TeV Pb-Pb collision Monte-Carlo data sample. For this analysis, the new detector set-up has been used.[9] The results for the resolution are shown in figure 6.1 and the results for the invariant mass are shown in figure 6.2. In appendix A the analysis needed to obtain the average, μ, and standard-deviation, σ for the different p_T bins is shown.

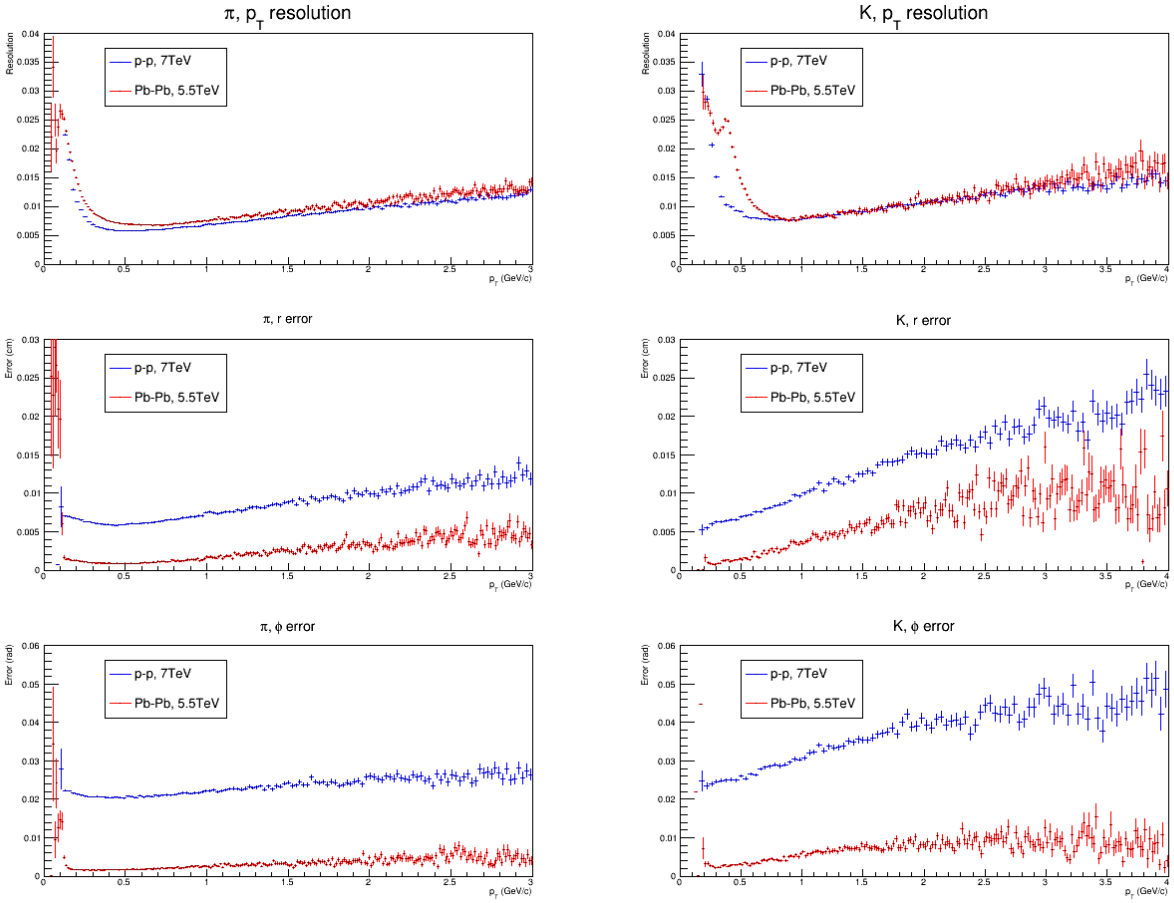

Figure 6.1: Comparison of the momentum resolution and positional error, in r (cm) and ϕ (rad), for p-p collisions at 7 TeV in the old detector set-up (blue) and Pb-Pb collisions at 5.5 TeV in the new detector set-up (red) for all pions and all kaons in the data sample.

[9]The results shown from these studies are obtained by M.K. van de Pas, a Bachelor student in our research group.

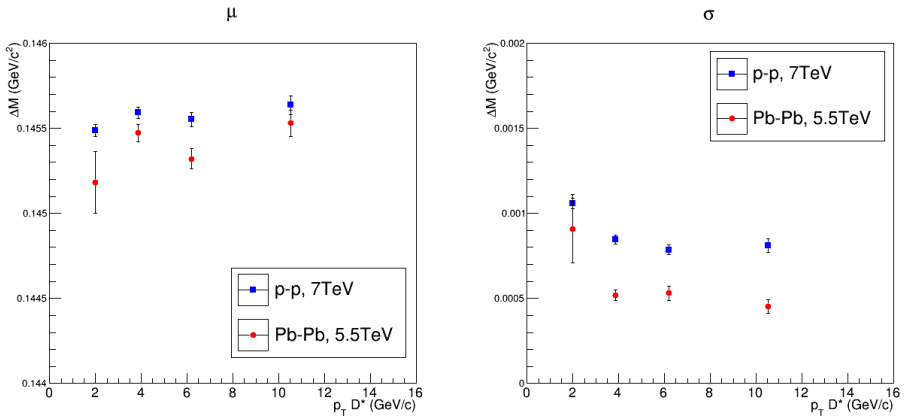

Figure 6.2: Comparison of the ΔM peak in p_T bins of the D^{*+}-meson for p-p collisions at 7 TeV in the old detector setup (blue) and Pb-Pb collisions at 5.5 TeV in the new detector setup (red) for all pions and all kaons in the data sample. Left: mean, μ, of the Gaussian peak. Right: width, σ, of the Gaussian peak.

As can be seen in figure 6.1, there is no improvement in the determination of the p_T of the pions and kaons. However, the improvement in the determination of the vertex of the pions and kaons is a factor 3 to 6, depending on the transverse momentum of the particle, and in angle it is even a factor 10. This is a very promising result for the cut on the impact parameter, since the measurement of the impact parameter depends on the measurement of these vertices.
From the invariant mass peaks (figure 6.2), we conclude that the average invariant mass difference is slightly lower for the Pb-Pb collisions. Also, the standard deviation is slightly lower. This last fact means that the peak is sharper, which implies that we can cut out background more effectively, since we can apply stricter cuts on the invariant mass difference. This will improve the statistical significance of the analysis.

6.2 Future studies

The results obtained in this thesis clearly showed the possibility to separate the prompt D^{*+}-mesons in a Monte-Carlo data set for p-p collisions at 7 TeV. Research has still to be done in order to optimize the cuts made on impact parameter. One could for instance look at more cut values. Interesting cut values would be 300 μm, 500 μm, 700 μm. Applying those extra cuts, will, together give a more complete picture of how fast the purity with respect to the cut values. In addition, these cut values might even give a purity of 100% for some of the p_T bins. This would imply that one can take a lower cut value to reach a purity of 100% and, hence, cut out less signal with the cut. Also, one could split the data in more or different p_T bins of the D^{*+}-meson. For this one should analyze a larger data-sample. For an optimal cut, one expects a high purity with respect to the prompt D^{*+}-mesons and a purity with respect to the combinatorial background that does not get too low. In addition, the statistical significances should be considerably larger than 1.
As discussed in the previous subsection, new data, that will be gathered in the coming years with the ALICE detector, might even allow us to get better result with the cuts for Pb-Pb collisions than the results found in this study. Applying the impact parameter cuts on real data will allow us to study the B-mesons in p-p collisions, where no quark-gluon plasma is created, and Pb-Pb collisions, where a quark-gluon plasma is created. This study will provide more insight into the properties of the quark-gluon plasma.

Appendix A Invariant mass distributions in p_T bins of the D^{*+}

In this appendix the invariant mass plots of the signal are shown. They are similar to plots shown in figure 3.1 and have, therefore, been put in the appendix. This appendix contains $\Delta M(D^{*+} - D^0)$ of the feed-down (figure A.1) and the prompt (figure A.2) in p_T bins of the D^{*+}-mesons, mentioned in section 3.3. In addition $\Delta M(D^{*+} - D^0)$ for the 2010 p-p collisions at 7 TeV (figure A.3) and for of the 5.5 TeV Pb-Pb collisions (figure A.4) in p_T bins of the D^{*+}-meson, mentioned in section 6.2, are shown here. The mean, μ, and standard deviation, σ, of the Gaussian fits have been shown in the respective chapters.

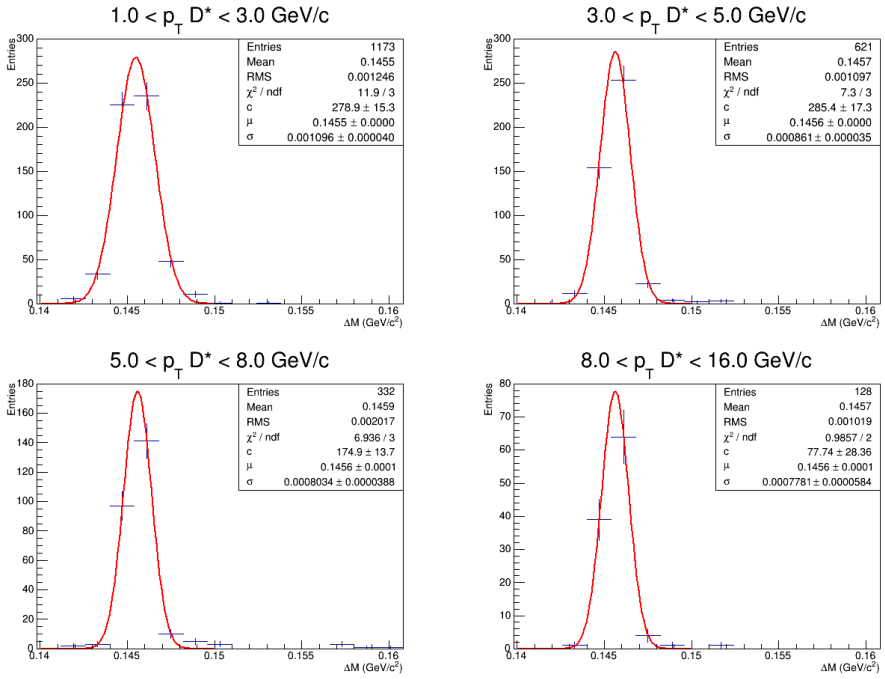

Figure A.1: Invariant mass difference distribution, ΔM, of the feed-down signal as measured by the ALICE detector in p_T bins of the D^{*+}-meson with Gaussian fits.

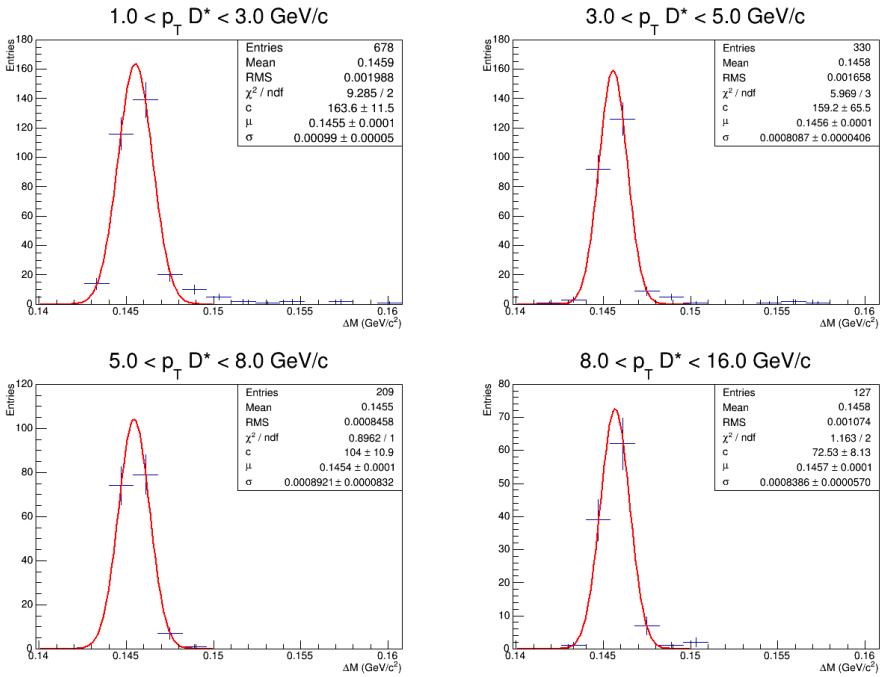

Figure A.2: Invariant mass difference distribution, ΔM, of the prompt signal as measured by the ALICE detector in p_T bins of the D^{*+}-meson with Gaussian fits.

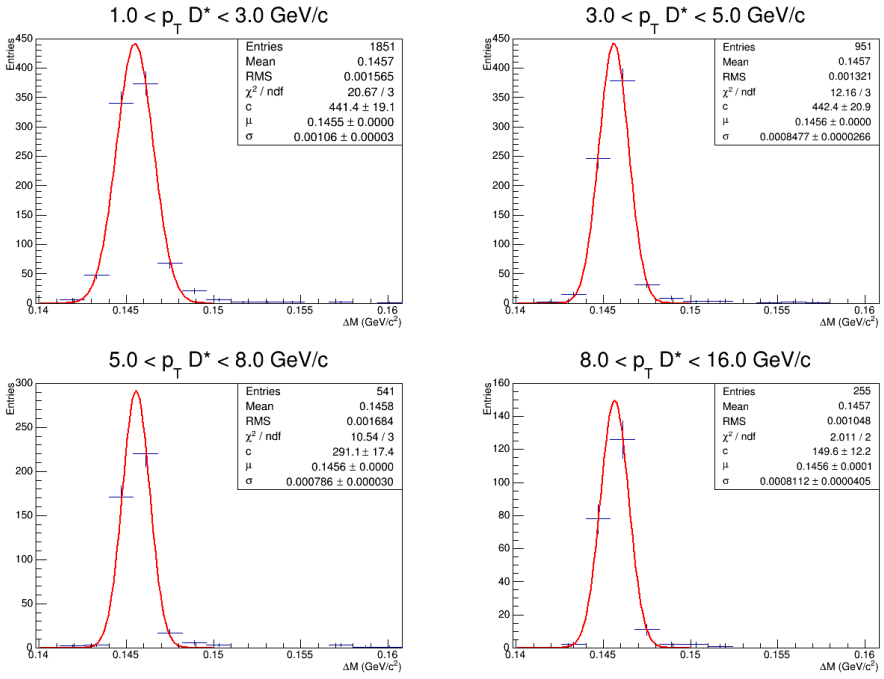

Figure A.3: Invariant mass difference distribution, ΔM, of the total signal as measured by the ALICE detector in p_T bins of the D^{*+}-meson for 7 TeV p-p collisions with Gaussian fits.

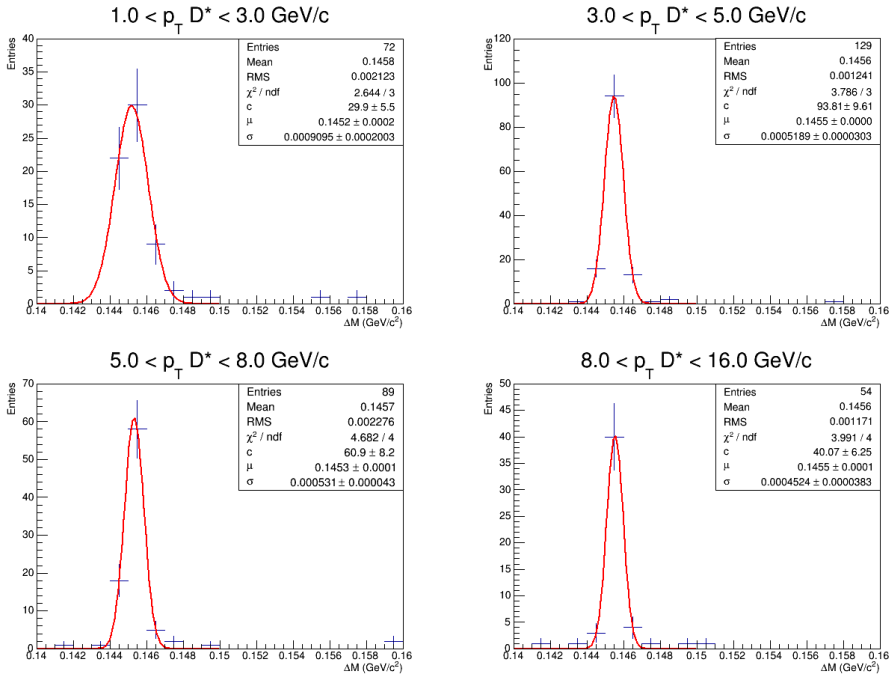

Figure A.4: Invariant mass difference distribution, ΔM, of the total signal as measured by the ALICE detector in p_T bins of the D^{*+}-meson for the 5.5 TeV Pb-Pb collisions with Gaussian fits.

Appendix B Momentum distributions of the D^{*+} daughters

In this appendix the transverse momentum distributions of all B-mesons (figure B.1) and of all D^0 (from D^{*+}), K (from D^0), π (from D^0) and π_s (from D^{*+}) (figure B.2) are shown. These distributions are less important for the main topic of this thesis, but give a good description of the data sample. Therefore, they have been put in this appendix.

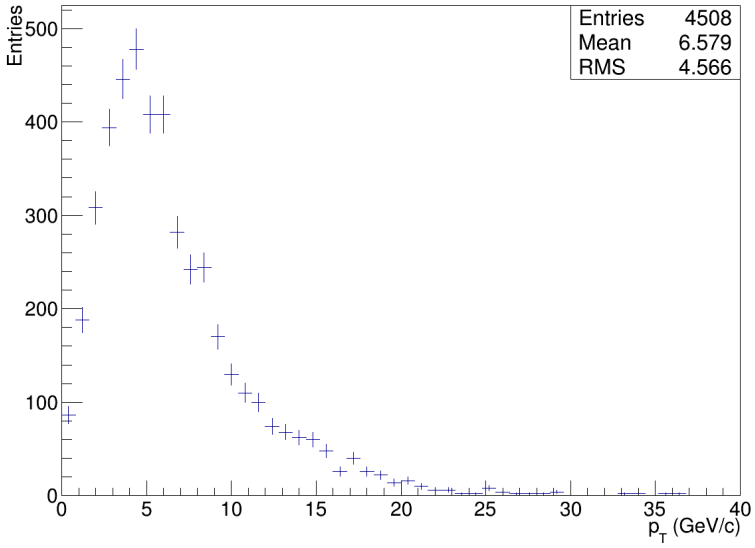

Figure B.1: Transverse momentum distribution of all B-mesons.

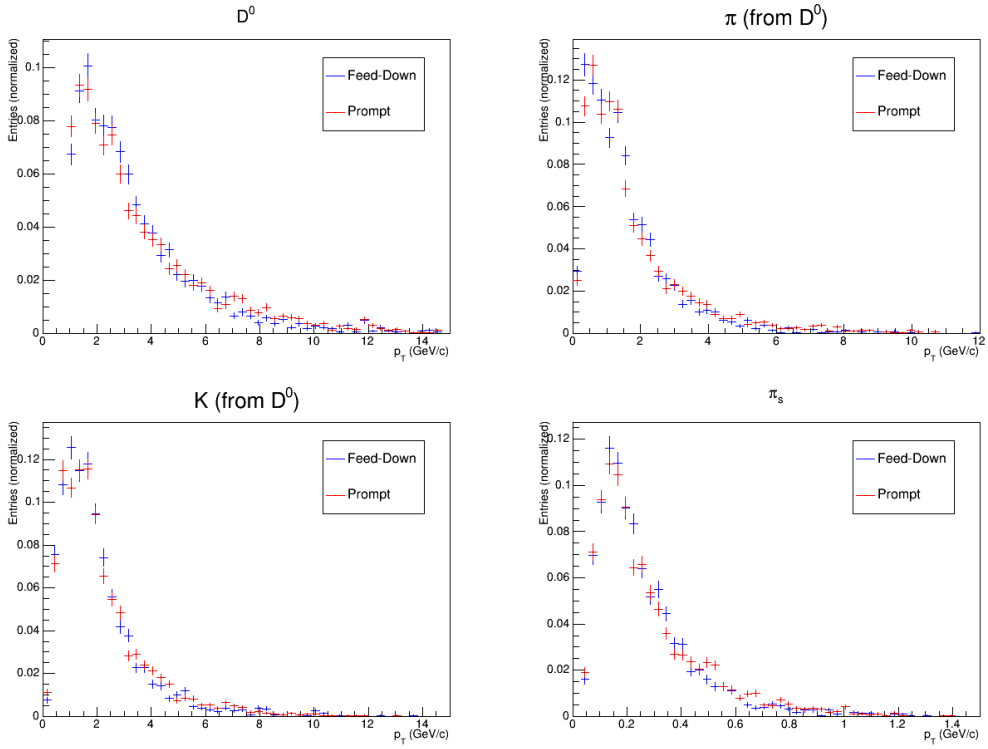

Figure B.2: Transverse momentum distributions of all D^0 (top left), π (from a D^0 decay) (top right), K (bottom left) and π_s (bottom right) mesons. A separation has been made between feed-down (blue) and prompt (red) mesons.

Appendix C Resolution of the detector

In order to study the difference in impact parameter of the feed-down and prompt D^{*+}-mesons, the detector should have a high enough resolution. As mentioned in section 2.1.1, the ITS detector is able to measure the vertex with an accuracy of 0.1 mm. To verify this, I calculated the difference between the real (or MC) vertex point (as can be found in the Monte-Carlo data set) and the measured (or reconstructed) vertex point (as can be found by analyzing the Monte-Carlo data set in the AliRoot framework). The resolutions in the transverse momentum, p_T, and the error in the radial distance, r, and the azimuthal angle, ϕ, for the π_s, K and π (from D^0 decays) mesons have been calculated by the formulas equations 17 and 18 and are shown in figure C.1.

$$Resolution = \left| \frac{Rec - MC}{MC} \right| \tag{17}$$

$$Error = \left| Rec \cdot \frac{Rec - MC}{MC} \right| \tag{18}$$

As can be seen in figure C.1, the resolution of the p_T-distribution is slightly increasing from 1% for low momenta to 4% for high momenta. In the resolution distribution for the soft pion, it can be seen that there are no soft pions with a momentum lower than $p_T = 0.1$ GeV/c. This can be explained by the fact that the magnetic field in the detector curves the track of the particles. For low momenta, the particles will not be able to reach the TPC, because of this magnetic field, and therefore, they cannot be reconstructed in the TPC. Hence, they will be cut out of the data by the TPC refit cut. For the soft pions the error in the radius is between 0.1 mm and 0.2 mm. The kaons and pions from D^0 decays have a larger uncertainty (i.e. about 0.15 mm for low momenta up to 0.4 mm for high momenta). The error in the angle is about 0.02 rad for the soft pions and about 0.04 rad for the kaons and pions from the D^0-meson. Hence, the error in the the angle will correspond to a distance of about 2% and 4% of the radius respectively. Assuming the B-meson flies 450 μm and the D^0-meson 100 μm, this will correspond to a maximum error of 11 μm and 22 μm, respectively. Hence, the total error in position will be about 200 μm for the soft pion and about 400 μm for the kaons and pions from D^0 decays. This error is about the same as the distance that a B-meson flies. This implies that the difference in impact parameter can be measured with enough statistics. The uncertainty is an order of magnitude too large to be able to see the difference in impact parameter directly. However, enough statistics should make the difference in the probability distributions visible.

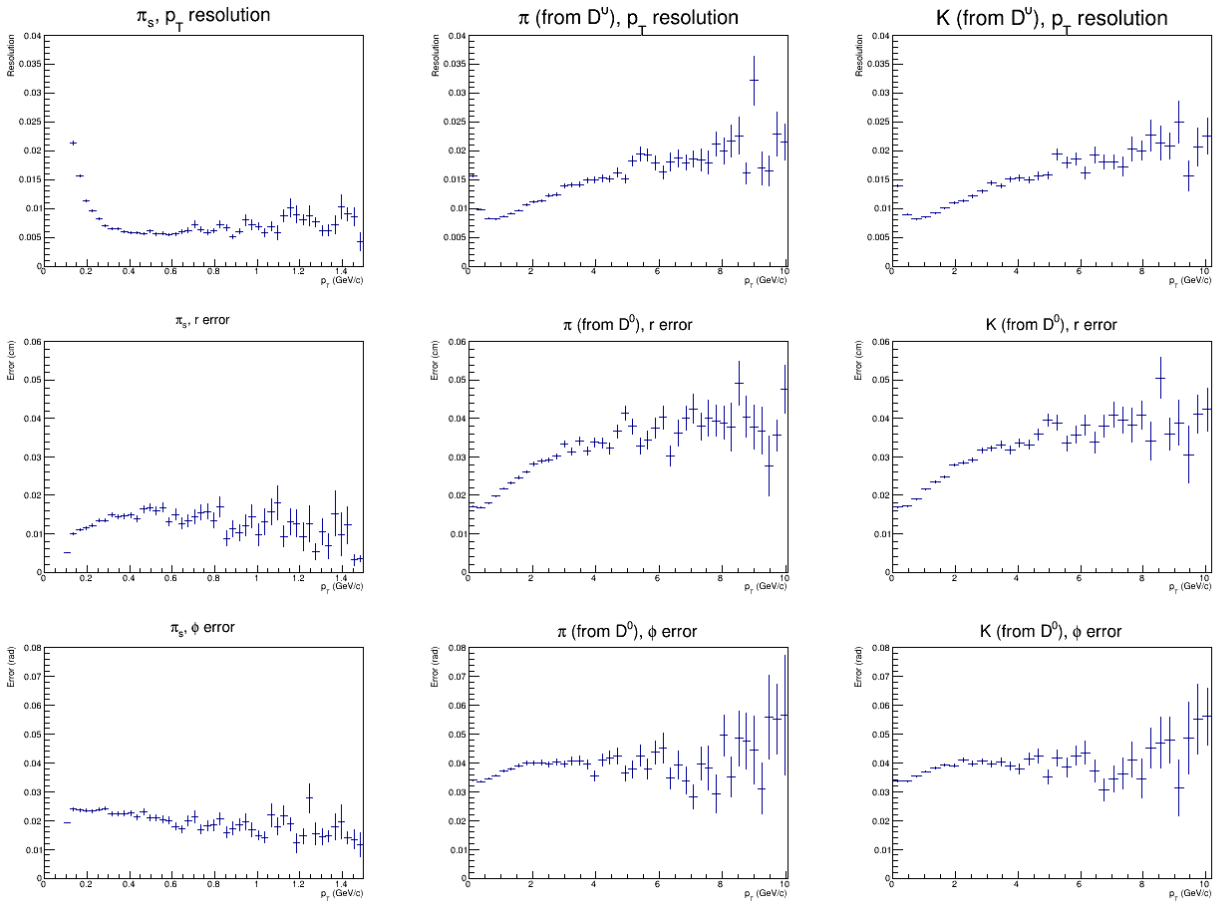

Figure C.1: Transverse momentum resolution (top row) and the positional error, in r (cm) (middle row) and ϕ (rad) (bottom row), for the π_s from D^{*+} decays (left column), π from D^0 decays (middle column) and K from D^0 decays (right column) meson decays.

References

[1] Symmetry Magazine: Dimensions of Particle Physics, http://www.symmetrymagazine.org/breaking/2010/11/18/first-measurements-public-from-lhc%25e2%2580%2599s-lead-ion-collisions - April 26, 2015.

[2] D. Griffiths, *Introduction to Elementary Particles*, John Wiley & Sons - 1987.

[3] R.S. de Rooij, *Prompt D^{*+} production in proton-proton and lead-lead collisions, measured at the CERN Large Hadron Collider*, Ph.D. Thesis, Utrecht University - 2013.

[4] L. Vermunt, *Performance studies for the measurement of B0 mesons in proton-proton collisions at 13 TeV with the ALICE experiment*, Bachelor Thesis, Utrecht University - January 2015.

[5] MissMJ, *Wikipedia: Standard Model*, http://upload.wikimedia.org/wikipedia/commons/0/00/Standard_Model_of_Elementary_Particles.svg - May 5, 2015.

[6] A.O. Sushkov, W.J. Kim, D.A.R. Dalvit, S.K. Lamoreaux, *New experimental limits on non-Newtonian forces in the micrometer-range*, arXiv:1108.2547 - August 12, 2011.

[7] B. Carithers, P. Grannis, *Discovery of the Top Quark*, Beam Line (SLAC) 25 (3): 416 - 1995.

[8] A. Pich, *Quantum Chromodynamics*, arXiv:hep-ph/9505231 - May 4, 1995.

[9] D. Leermakers, *Optimization of the reconstruction of $B0 \rightarrow D^{*+}$ pi^- and $D^{*+} \rightarrow D0$ pi^+ decays with the ALICE detector*, Bachelor Thesis, Utrecht University - June 18, 2014.

[10] C. Bal, *Elementary Particles*, http://u2.lege.net/cetinbal/elementaryparticles.htm - May 6, 2015.

[11] K. McNulty Walsh, *Tracking the Transition of Early-Universe Quark Soup to Matter-as-we-know-it*, http://www.bnl.gov/rhic/news2/news.asp?a=4473&t=today, Brookhaven National Laboratory: Relativistic Heavy Ion collider - April 4, 2014.

[12] A. Toia, *Participants and spectators at the heavy-ion fireball*, http://cerncourier.com/cws/article/cern/53089, Cern Courier - April 26, 2013.

[13] S.R. Soltz, *A Question of Quarks*, https://str.llnl.gov/str/JanFeb03/Soltz.html, Science and Technology Review - May 5, 2015.

[14] T. Song, C.M. Ko, S.H. Lee, *Quarkonium formation time in quark-gluon plasma*, arXiv:1302.4395 - February 18, 2013.

[15] Yu.L. Dokshitzer, D.E. Kharzeev, *Heavy quark colorimetry of QCD matter*, Phys.Lett.B519:199-206 - 2001.

[16] ZEUS Collaboration, *Measurement of charm fragmentation fractions in photoproduction at HERA*, arXiv:1306.4862 - June 20, 2013.

[17] K.A. Olive et al. (Particle Data Group), *Review of Particle Physics*, Chin. Phys. C, 38 - January 15, 2014.

[18] U. Egede, *Pattern recognition in the Inner Detector*, http://www.hep.lu.se/atlas/thesis/egede/thesis-node81.html - August 1, 1998.

[19] CERN, *About CERN*, http://home.web.cern.ch/about - May 23, 2015.

[20] The ALICE collaboration, *The ALICE detectors*, http://alipub-dev.web.cern.ch/ - May 23, 2015.

[21] The ALICE collaboration, *The ALICE experiment*, http://aliceinfo.cern.ch/Public/en/Chapter2/Chap2Experiment-en.html - 2008.

[22] The ALICE collaboration, *Alignment of the ALICE Inner Tracking System with cosmic-ray tracks*, JINST 5: P03003 - 2010.

[23] C. Lippman, *Particle identification in ALICE: an extra boost in QGP studies - Part B*, http://alicematters.web.cern.ch/?q=CL_PID2 - October 13, 2012.

[24] The ALICE Collaboration, *High p_t identified particle production in ALICE*, Nucl.Phys. A910-911 (2013) 20-26 - August, 2013.

[25] R. Brun, F. Rademakers, *ROOT - An object oriented data analysis framework*, Nuclear Instruments and Methods in Physics Research Section A: Accelerators, Spectrometers, Detectors and Associated Equipment, Volume 389, Issues 1-2, Pages 81-86 - April 11 1997.

[26] F. Colomaria, *Measurements of D0 production from Kpipipi decay channel*, https://twiki.cern.ch/twiki/bin/view/Sandbox/FabioColamariaSandbox - January 26, 2012.

[27] B. Abelev et al. (ALICE Collaboration), *Suppression of high transverse momentum D mesons in central Pb-Pb collisions at* $\sqrt{s_{NN}} = 2.76$ *TeV*, arXiv:JHEP09(2012)112 - March, 2012.

[28] A. Grelli, Y. Wang, C. Ivan (The ALICE off-line Project), *AliAnalysisTaskSEDStarSpectra*, ALICE Experiment at CERN, 1998-2009.